The Astrophysical Journal, 985:110 (22pp), 2025 May 20 https://doi.org/10.3847/1538-4357/adbc61

Modeling Triatomic Biosignatures: Ozone and Isotopomers

Thomas M. Cross[1], David M. Benoit[1], and Marco Pignatari[1,2,3,4,5]
[1] E. A. Milne Centre for Astrophysics, Department of Physics and Mathematics, University of Hull, Hull, HU6 7RX, UK; T.Cross-2019@hull.ac.uk
[2] Konkoly Observatory, Research Centre for Astronomy and Earth Sciences, HUN-REN, Konkoly Thege Miklós út 15-17, H-1121 Budapest, Hungary
[3] CSFK, MTA Centre of Excellence, Budapest, Konkoly Thege Miklós út 15-17, H-1121, Hungary
[4] Joint Institute for Nuclear Astrophysics—Center for the Evolution of the Elements, USA
Received 2024 March 8; revised 2025 February 25; accepted 2025 March 1; published 2025 May 16

Abstract

In this work, we present a new approach to produce spectroscopic constants and model first-principles synthetic spectra for all molecules of astrophysical interest. We have generalized our previous diatomic molecule simulation framework, employing transition-optimized shifted Hermite (TOSH) theory, thereby enabling the modeling of polyatomic rotational constants for molecules with three or more atoms. These capabilities are now provided by our new code Epimetheus. As a first validation of our approach, we confront our predictions and assess their accuracy against the well-studied triatomic molecule ozone 666 ($^{16}O_3$), in addition to eight of its potential isotopomers: ozone 668 ($^{16}O^{16}O^{18}O$), 686 ($^{16}O^{18}O^{16}O$), 667 ($^{16}O^{16}O^{17}O$), 676 ($^{16}O^{17}O^{16}O$), 688 ($^{16}O^{18}O^{18}O$), 868 ($^{18}O^{16}O^{18}O$), 888 ($^{18}O_3$), and 777 ($^{17}O_3$). We then assess the accuracy of these rotational constants using the Epimetheus data in our code Pandora, and generate synthetic molecular spectra. The ozone spectra presented here are purely infrared and not Raman. Epimetheus builds upon the work from our previous code Prometheus, which used the TOSH theory to account for anharmonicity for the fundamental $\nu = 0 \rightarrow \nu = 1$ band, going further to now account for triatomic molecules. This is combined with thermal profile modeling for the rotational transitions. We have found that this extended method performs well, typically approximating the spectroscopic constants with errors of less than 2%. Some issues do arise depending on the symmetry group of the ozone isotopomer. From these spectroscopic constants and using our own spectral modeling code, we show that we can provide the data to produce appreciable molecular spectra, which are good approximations until high-resolution studies can be done.

Unified Astronomy Thesaurus concepts: Biosignatures (2018); Astrochemistry (75)

1. Introduction

This work provides an extension to the methodology described in our previous paper to model biosignatures (T. M. Cross et al. 2022). Molecular lines are ideal observation targets to study biosignatures in exoplanetary atmospheres. However, apart from extremely well-studied molecules, the basic data needed to detect most biosignatures is incomplete. We aim now to extend past the diatomic molecules explored previously and produce spectroscopic constants (and to a lesser degree spectra) for polyatomic molecules. Specifically, within this paper we will be focusing first on a triatomic molecule, with an extension to other triatomics and larger polyatomic molecules in future publications. Like before, we are trying to address the methodological gap between approximate, fundamental-only models (such as harmonic; e.g., K. O. H. M. Dundas et al. 2021), and labor-intensive, extremely accurate line lists (such as ExoMol and HITRAN; see, e.g., J. Tennyson et al. 2020 and I. E. Gordon et al. 2022). This is an area of research which has begun to garner interest, as the rapid production of vibrational spectral data is paramount for the identification of molecules in exoplanetary atmospheres (J. C. Zapata Trujillo et al. 2023).

Generally, a biosignature is defined as an object, substance, and/or pattern whose origin specifically requires a biological agent (D. J. D. Marais & M. R. Walter 1999). In the context of astronomical observations, however, this is used to mean a gas that is produced by life and accumulates in a planet's atmosphere. An ideal biosignature would be unambiguous, with living organisms being its unique source (J. S. Greaves et al. 2020). In reality, though, many biosignatures can be also produced through abiotic processes and therefore can act as false positives (C. E. Harman & S. Domagal-Goldman 2018). There is currently no globally accepted scheme for classifying what molecules are potentially atmospheric biosignatures (E. W. Schwieterman et al. 2018), which means we have to select one.

In this work, we have opted to use a scheme by S. Seager et al. (2016), who through a cross-discipline scientific effort have created a list called "The All Small Molecules" catalog (ASM), which contains over 16,000 potential biosignature molecules. Out of the potential pool of candidates within the ASM, we have selected ozone as our test case for this study. This was done for a variety of reasons. First, the fact that ozone is an asymmetric top (for more details, see S. Mikhailenko et al. 1999), and thus differs from a linear triatomic molecule such as carbon dioxide (CO_2), which would effectively model like a simpler diatomic (see our previous approach in T. M. Cross et al. 2022). Additionally, ozone has been thoroughly investigated, and plenty of experimental data are available for us to benchmark our synthetic data (R. Gamache 1985; L. Rothman et al. 1987; J.-M. Flaud et al. 1990, 2003; C. P. Rinsland et al. 1991; J. Flaud & R. Bacis 1998; B. C. Hathorn & R. A. Marcus 2001; G. Wagner et al. 2002; A. Barbe et al. 2018; I. Gayday et al. 2020; V. Tyuterev et al. 2021; I. E. Gordon et al. 2022).

It is known that on Earth ozone appears throughout the entire atmosphere, but resides prominently in a layer in the lower

[5] NuGrid Collaboration, http://nugridstars.org

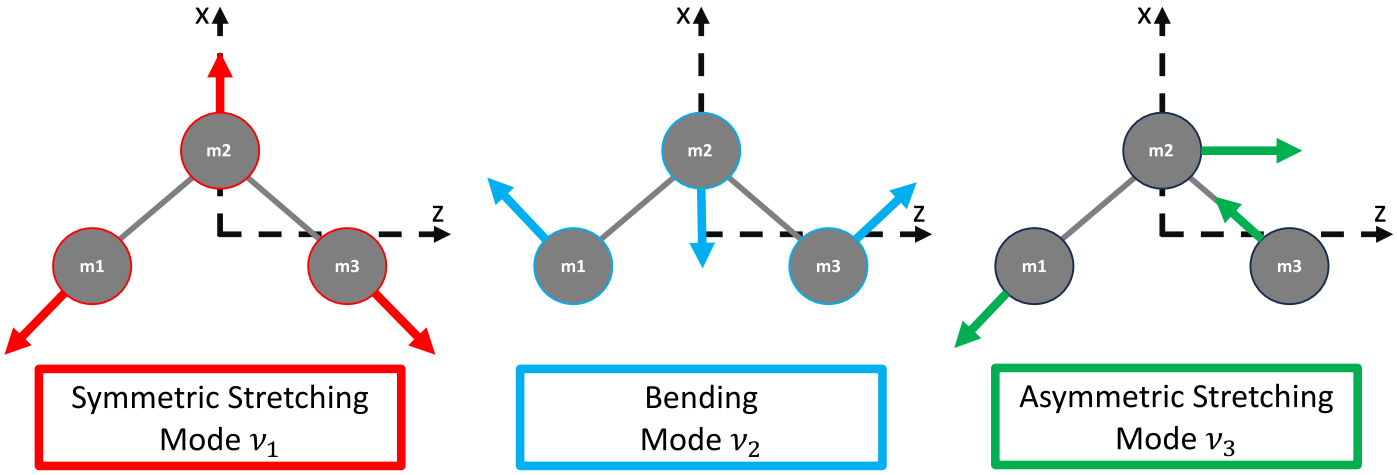

Figure 1. The three vibrational normal modes for a nonlinear triatomic such as ozone.

stratosphere at an altitude between 15 and 30 km (R. G. Prinn et al. 1978). Ozone is crucial for our atmosphere as it is responsible for the temperature inversion effect within the stratosphere (L. Kaltenegger 2011), where temperature is reliant upon the solar energy absorbed. This ultimately means this stratospheric ozone reduces the incoming ultraviolet radiation (S. Solomon 1999) to levels acceptable for not only life's development but also its continuation (F. Montmessin et al. 2011).

Ozone is also important because of its relationship to another key biosignature: diatomic oxygen (O_2). On Earth, O_2 is produced from oxygenic photosynthesis, whether it be via flora or fauna, by for example cyanobacteria (M. Battistuzzi et al. 2023). Ozone is created photochemically in the atmosphere from O_2, consequently meaning its concentration depends heavily upon the production of O_2 (S. D. Domagal-Goldman et al. 2014). The reactions which naturally form and destroy ozone, known as the Chapman reactions (S. Chapman 1930), are described in Equations (1), (2), (3), and (4) below (please note that species "M" in these equations denotes a third body required to carry away excess vibrational energy):

$$O_2 + h\nu \rightarrow 2O, \quad (1)$$

$$O + O_2 + M \rightarrow O_3 + M, \quad (2)$$

$$O_3 + h\nu \rightarrow O_2 + O, \quad (3)$$

$$O_3 + O \rightarrow O_2 + O_2. \quad (4)$$

This is not the only means of production of O_2, as it can be formed abiotically in atmospheres with high concentrations of CO_2 (A. Segura et al. 2007; J. Grenfell et al. 2013). Abiotic sources of ozone have been detected on two terrestrial planets within our solar system, Mars (K. E. Fast et al. 2009; K. S. Olsen et al. 2020) and Venus (F. Montmessin et al. 2011; E. Marcq et al. 2019), both of which are currently understood to be uninhabited by life. Further studies have shown that the ozone in the atmosphere of Mars has been produced from the photolysis of the high levels CO_2 (F. Lefèvre et al. 2021) and then the Chapman reactions (S. Chapman 1930), thus confirming an example of ozone's creation from abiotic means. Minor traces of ozone have also been detected on the Jupiter moon Ganymede (K. S. Noll et al. 1996).

From a physical chemistry standpoint, ozone is a bent asymmetric rotor. The "symmetric" isotopic variants (such as $^{16}O_3$) belong to the C_{2V} point symmetry group, and the "asymmetric" species (such as $^{16}O^{16}O^{18}O$) belong to the C_S point group (S. Mikhailenko et al. 1999). This is important as the differences in symmetry point groups has an appreciable effect on the possible energetic transitions accessible to each species, in turn altering the spectra produced, and will be discussed further in Section 2.5.

The vibrational states of ozone are usually described using three quantum numbers, n_1, n_2, and n_3. These are often written simply as "$n_1n_2n_3$." Each of these quantum numbers describes the degree of excitation of the three normal modes: the symmetric stretch ν_1, bend ν_2, and asymmetric stretch ν_3 (C. N. Banwell 1972). For example, the band "001" describes when ozone has a single excitation in the asymmetric stretch vibration, ν_3, but no excitation in the symmetric stretch and bending vibration. Bands which contain only a single excitation in one type of vibration are known as fundamental bands, and are the focus of this paper. The normal modes of vibration for the fundamental bands of ozone (100, 010, and 001, in this case) are shown in Figure 1.

The isotopic variants for which we investigate band origins, rotational constants, and spectra are shown in Table 1. The order of these variants has been decided by their abundance, starting with the most abundant and then in decreasing order. The other isotopologs not shown in Table 1 are presented in Section 3.2, but have only been evaluated by their band origins. For a full abundance list with all 18 stable isotopologs, please refer to Table 2 of A. Barbe et al. (2022). Table numbers corresponding to the isotopologs' spectroscopic constants are included Table 1, as well as figure numbers for the corresponding spectra.

In Section 2, we introduce the methodology and theory required to derive the spectroscopic constants, which is used within our code, Epimetheus. The last portion of the methodology, Section 2.5, gives a brief description of the method used to model the rovibrational spectra. A more detailed account of our spectral modeling approach (Pandora) will be published in a separate paper. In Section 3, we discuss our results and compare them with the literature. Section 4 presents generated rovibrational spectra using data obtained in Section 3, with comparisons to well-established databases. The most significant features are summarized for each isotopomer. We conclude our findings in Section 5. Links to the codes used within this work can be found in the Code Availability section.

Table 1
List of Ozone Isotopomers and Their Natural Abundances, Truncated to Include Only the Variants Included within the Major Data Reported within This Paper

Isotopic Species	Designation	Spins of Atoms	Natural Abundance	Table No.	Spectra Figure(s)
$^{16}O_3$	666	0 0 0	0.992901	2	3, 4, 2
$^{16}O^{16}O^{18}O$	668	0 0 0	3.98194×10^{-3}	2	6(A)
$^{16}O^{18}O^{16}O$	686	0 0 0	1.99097×10^{-3}	3	6(B)
$^{16}O^{16}O^{17}O$	667	$0\ 0\ \frac{5}{2}$	7.40475×10^{-4}	3	6(C)
$^{16}O^{17}O^{16}O$	676	$0\ \frac{5}{2}\ 0$	3.70237×10^{-4}	4	7(A)
$^{16}O^{18}O^{18}O$	688	0 0 0	8.384576×10^{-6}	4	⋯
$^{18}O^{16}O^{18}O$	868	0 0 0	4.192288×10^{-6}	5	7(B)
$^{18}O_3$	888	0 0 0	8.615×10^{-9}	5	7(C)
$^{17}O_3$	777	$\frac{5}{2}\ \frac{5}{2}\ \frac{5}{2}$	5.5×10^{-11}	6	⋯

Note. All data have been obtained from A. Barbe et al. (2022). The designation column refers to the abbreviation that the isotopolog may be given throughout this paper.

2. Methodology

This section details the novel approach implemented in our new code Epimetheus. Compared to our previous paper T. M. Cross et al. (2022), we developed a more general methodology to obtain the anharmonically corrected spectroscopic constants for polyatomic molecules. This includes the band origin for each of the fundamental vibrational modes and the three rotational constants A, B, and C, as opposed to the singular B rotational constant for diatomic molecules (R. W. Field 2015).

We also briefly discuss the process by which we model the spectroscopic constants, and also show the key equations required to produce a spectrum. As the spectral modeling is done using our other code—Pandora—and the prominent focus of our study relates to the anharmonic corrections of spectroscopic constants, we will not go into too much detail here. The in-depth spectral modeling methodology will be explained in a later paper, however the code is provided here should these results wish to be reproduced.

Finally, we describe the computational details of our method. This ranges from the choices of inputted data to the choice of method used to calculate anharmonic correction variables.

2.1. Determination of the Band Origins

To calculate the anharmonic corrections, we first compute a Hessian matrix $\boldsymbol{f}_{\mathbf{CART}}$ (J. W. Ochterski 1999), which contains the second partial derivatives of the potential, V, with respect to displacement of the atoms in Cartesian (CART) coordinates:

$$f_{\mathrm{CART}ij} = \left(\frac{\partial^2 V}{\partial \xi_i \partial \xi_j}\right)_0. \tag{5}$$

The matrix is $3N \times 3N$ in size, where N is the number of atoms within a molecule. ξ_1, ξ_2, ξ_3, ⋯, ξ_{3N} are used to represent the displacement in Cartesian coordinates, Δx_1, Δy_1, Δz_1, ⋯, Δz_N. The $()_0$ is used to indicate that the derivatives are taken at the equilibrium positions of the atoms, and therefore the first derivatives are assumed to be zero. The matrix created by the Hessian is shown below in Equation (6):

$$\boldsymbol{f}_{\mathbf{CART}} = \begin{pmatrix} \frac{\partial^2 V}{\partial \xi_1 \partial \xi_1} & \frac{\partial^2 V}{\partial \xi_1 \partial \xi_2} & \frac{\partial^2 V}{\partial \xi_1 \partial \xi_3} & \cdots & \frac{\partial^2 V}{\partial \xi_1 \partial \xi_n} \\ \frac{\partial^2 V}{\partial \xi_2 \partial \xi_1} & \frac{\partial^2 V}{\partial \xi_2 \partial \xi_2} & \frac{\partial^2 V}{\partial \xi_2 \partial \xi_3} & \cdots & \frac{\partial^2 V}{\partial \xi_2 \partial \xi_n} \\ \vdots & \vdots & \vdots & \ddots & \vdots \\ \frac{\partial^2 V}{\partial \xi_n \partial \xi_1} & \frac{\partial^2 V}{\partial \xi_n \partial \xi_2} & \frac{\partial^2 V}{\partial \xi_n \partial \xi_3} & \cdots & \frac{\partial^2 V}{\partial \xi_n \partial \xi_n} \end{pmatrix}. \tag{6}$$

In our implementation, we use the method derived by C. Y. Lin et al. (2008) in their transition-optimized shifted Hermite (TOSH) theory to compute the Hessian matrix. The equations to describe the elements under this framework are included in Section 2.6.

The next step is to appropriately mass-weight the calculated second derivatives to convert them into mass-weighted coordinates (MWC):

$$f_{\mathrm{MWC}ij} = \frac{f_{\mathrm{CART}ij}}{\sqrt{m_i m_j}} = \left(\frac{\partial^2 V}{\partial q_i \partial q_j}\right)_0, \tag{7}$$

where $q_i = \sqrt{m_i}\xi_i$ is the mass-weighted Cartesian coordinate for ξ_i. The MWC Hessian is the following:

$$\boldsymbol{f}_{\mathbf{MWC}} = \begin{pmatrix} \frac{\partial^2 V}{\partial q_1 \partial q_1} & \frac{\partial^2 V}{\partial q_1 \partial q_2} & \frac{\partial^2 V}{\partial q_1 \partial q_3} & \cdots & \frac{\partial^2 V}{\partial q_1 \partial q_9} \\ \frac{\partial^2 V}{\partial q_2 \partial q_1} & \frac{\partial^2 V}{\partial q_2 \partial q_2} & \frac{\partial^2 V}{\partial q_2 \partial q_3} & \cdots & \frac{\partial^2 V}{\partial q_2 \partial q_9} \\ \vdots & \vdots & \vdots & \ddots & \vdots \\ \frac{\partial^2 V}{\partial q_9 \partial q_1} & \frac{\partial^2 V}{\partial q_9 \partial q_2} & \frac{\partial^2 V}{\partial q_9 \partial q_3} & \cdots & \frac{\partial^2 V}{\partial q_9 \partial q_9} \end{pmatrix}. \tag{8}$$

Once the MWC Hessian has been obtained, the normal modes $\boldsymbol{Q}_i$ (eigenvectors), and corresponding harmonic vibrational frequencies ω_i (eigenvalues), are obtained by diagonalizing $\boldsymbol{f}_{\mathbf{MWC}}$. Since the lowest eigenvectors will correspond to global translations or rotations of the molecule (six modes for a nonlinear molecule and five for a linear molecule), we only

consider the $M = 3N - 6$ or $M = 3N - 5$ eigenvectors associated with the largest eigenvalues. Those eigenvalues can be converted in wavenumbers using the conversion described in Equation (9) below:

$$\omega_i = \sqrt{\frac{\eta_{ii}}{4\pi^2 c_{\rm cm}^2}}. \tag{9}$$

The constant $c_{\rm cm}$ is the speed of light, and η_{ii} is the eigenvalue and ω_i the harmonic frequency of mode i. To be able to obtain ω in wavenumbers (in reciprocal centimeters, $\rm cm^{-1}$), $c_{\rm cm}$ must have units of inverse square centimeters per second ($\rm cm^{-2}\,s^{-1}$) and η_{ii} must be in units of joules per square meter per kilogram ($\rm J\,m^{-2}\,kg^{-1}$).

We use Equation (9) to computed the harmonic frequencies for each of the fundamental modes. The next step, detailed in Section 2.2, is to calculate further spectroscopic constants required to include anharmonic correction for those frequencies.

It is worth noting that throughout this work we have made the assumption of Eckart frames for the molecular frame, with the equilibrium frame chosen at the principle axis system, as is typically the standard practice for defining the normal modes.

2.2. Anharmonically Correcting the Band Origins

We will now detail the process of correcting the band origins that have been calculated by the eigenvalues in Equation (7). C. Y. Lin et al. (2008) stated that, for polyatomic molecules, the TOSH fundamental transition energy for the ith mode is described as

$$\Delta E_i^{\rm TOSH} = \omega_i + \frac{1}{8\omega_i}\sum_j^M \frac{\eta_{iijj}}{\omega_j} + \frac{1}{2\omega_i}\sum_j^M \eta_{iij}\sigma_{ij} + \frac{1}{4\omega_i}\sum_j^M \eta_{iijj}\sigma_{ij}^2. \tag{10}$$

where η_{iijj} is the quartic constant, η_{iij} is the cubic constant, and σ_{ij} is a shift parameter (see below and also C. Y. Lin et al. 2008). The method we use to compute the cubic and quartic constants is detailed in Section 2.6.

A key term in this equation is σ, which is the parameter providing the shift to the harmonic oscillator functions from their equilibrium position, thus providing anharmonic corrections. The equation to calculate σ differs from the one shown in our previous paper (T. M. Cross et al. 2022), since we now need a σ that can accurately represent the multi-mode nature of a polyatomic molecule as opposed to a single-mode diatomic.

σ is calculated by comparing Equation (10) with the second-order perturbation theory (VPT2) equation for the polyatomic fundamental energy difference. It is described by the following:

$$\sigma_{ij} = \frac{(\delta_{ij} - 2)(\omega_i + \omega_j)\eta_{iij}}{4\omega_i\omega_j^2(2\omega_i + \omega_j)} - \sum_k^M \frac{\eta_{kkj}}{4\omega_k\omega_j^2}. \tag{11}$$

The variable δ_{ij} in this equation represents the Kronecker delta, where $\delta_{ij} = 0$ occurs when $i \neq j$ and when $i = j$ it becomes $\delta_{ij} = 1$. The notation here of η_{kkj} does not imply $k \neq i$ in the summation component of Equation (11). The σ_{ij} elements define the σ matrix, which has dimensions of $M \times M$. A key detail to note is the TOSH formulation uses fewer terms than the VPT2 methodology; in particular, it does not use the η_{ijk} derivative as shown by Table 1 in C. Y. Lin et al. (2008). This has the natural implication that temporal and computational cost is cheaper for the TOSH method than VPT2.

2.3. Obtaining the Polyatomic Rotational Constants

Before we begin the anharmonic corrections to the equilibrium geometries, we first need to calculate geometries with respect to the center of mass (COM). The first step is to actually calculate the COM, which is done using the typical equations. For a complete example workout, see Appendix A, where we run through how the COM is calculated for an imaginary molecule ($\alpha\beta\gamma$). $\alpha\beta\gamma$ has been selected for a work through rather than O_3 as it is easier to differentiate between the atoms.

We then calculate the moments of inertia (diagonal elements) and the products of inertia (nondiagonal elements) of the moment of inertia tensor $\boldsymbol{I}$. This is represented by Equation (12) below (for a complete breakdown on how to calculate each component within the moment of inertia tensor $\boldsymbol{I}$, such as I_{xx}, of the inertia tensor, please refer to Appendix B):

$$\boldsymbol{I} = \begin{pmatrix} I_{xx} & I_{xy} & I_{xz} \\ I_{yx} & I_{yy} & I_{yz} \\ I_{zx} & I_{zy} & I_{zz} \end{pmatrix}. \tag{12}$$

The inertia matrix can be diagonalized into its corresponding eigenvalues (also known as the principal moments of inertia) and eigenvectors. As there are three eigenvalues, we will obtain three rotational constants, A, B, and C. These have the following relations to define them by:

$$A = \frac{\hbar}{4\pi c_{\rm cm} I_A} > B = \frac{\hbar}{4\pi c_{\rm cm} I_B} > C = \frac{\hbar}{4\pi c_{\rm cm} I_C} \quad \therefore \quad I_C > I_B > I_A. \tag{13}$$

Like Equation (9), $c_{\rm cm}$ represents the speed of light, which as previously mentioned needs to be in specific units ($\rm cm\,s^{-1}$) rather than the usual meters per second ($\rm m\,s^{-1}$) units to ultimately produce rotational constants with wavenumber units. $\hbar$ represents the reduced Planck constant, which is given in units of J s. Once again, awareness need to be exercised with regards to the units as the eigenvalues will need to be in the correct unit form (square meters kilogram, $\rm m^2\,kg$), for Equation (13) to produce rotational constants in the form of wavenumbers ($\rm cm^{-1}$).

2.4. Anharmonically Correcting the Polyatomic Rotational Constants

Similar to our previous work (T. M. Cross et al. 2022), we assume that the harmonic shift matrix $\boldsymbol{\sigma}$, defined by Equation (11), captures the geometric changes caused by anharmonicity. Indeed, we showed for diatomics that shifting the equilibrium geometry by σ (in that case a scalar) led to a good approximation of the vibrationally averaged geometry for the first excited vibrational state for diatomics. The shifted geometry enabled us to determine B_1 for that excited state to less than a percent in most cases. We present here a generalization of this approach to all polyatomic molecules.

First, to simplify the notation, we define an excitation vector as

$$\boldsymbol{n} = \begin{pmatrix} n_1 \\ n_2 \\ \vdots \\ n_M \end{pmatrix}, \tag{14}$$

where n_i represents the excitation quanta in mode i. For example, the ground state is defined as an M-dimensional zero vector, $\mathbf{0}$. To compute the geometry distortion caused by a single excitation in mode j, denoted by excitation vector $\boldsymbol{n}_j$, we compute the matrix-vector product:

$$\boldsymbol{\sigma n}_j = \begin{pmatrix} \sigma_{1j} \\ \sigma_{2j} \\ \vdots \\ \sigma_{Mj} \end{pmatrix}. \tag{15}$$

Here we assume that only mode j is excited and all other modes are in their ground state. The matrix-vector product expression remains valid for other excitation patterns, but the resulting vector will have a more complex expression. To further clarify the excitation pattern used, we index the variables with $0 \ldots n_j \ldots 0$ to represent the chosen excitation.

This resulting shift vector is expressed in the basis of the normal-mode vectors determined earlier in Section 2.1, and therefore the corresponding Cartesian displacement, $\boldsymbol{\sigma}_{0\cdots n_j\cdots 0}$, can be written as

$$\boldsymbol{\sigma}_{0\cdots n_j\cdots 0} = \sigma_{1j}\,\boldsymbol{Q}_1 + \sigma_{2j}\,\boldsymbol{Q}_2 + \cdots + \sigma_{Mj}\,\boldsymbol{Q}_M, \tag{16}$$

where the $\boldsymbol{Q}_i$ are the Cartesian normal-mode eigenvectors obtained in Section 2.1.

Finally, the displaced Cartesian geometry for a single excitation in mode n_j is computed using the equilibrium Cartesian geometry $\boldsymbol{X}_0$ as

$$\boldsymbol{X}_{0\cdots n_j\cdots 0} = \boldsymbol{X}_0 + \boldsymbol{\sigma}_{0\cdots n_j\cdots 0}. \tag{17}$$

Note that since we are using normal modes as displacement vectors, the COM position remains unaffected by construction and the frame orientation is also conserved. Using this new displaced nuclear configuration, we can obtain new rotational constants by recomputing the inertia tensor and following the procedure outlined earlier in Section 2.3. The entire process described then needs to be repeated for every modal excitation.

Since the ground-state excitation vector is a zero vector (i.e., $\boldsymbol{\sigma}_{0\cdots 0} = \mathbf{0}$), the geometry used for the ground-state rotational constants is the equilibrium Cartesian geometry $\boldsymbol{X}_0$, as suggested for diatomic molecules in T. M. Cross et al. (2022).

2.5. Spectral Modeling Overview

In this section, we describe the process of modeling the spectra used with our other code, Pandora. This ranges from deriving the possible transitions to the intensities of those transitions. We will only cover the essentials here and provide useful references for the reader to investigate should they wish to do so.

For the infrared rotational spectrum, provided a permanent dipole moment is present (G. Herzberg 1945), the selection rule for the J quantum number is $J = 0, \pm 1$. Therefore, only the equations for the P, Q, and R branches are needed. It is worth noticing that the following branch equations have been derived to accurately describe ozone, which is an asymmetric top molecule and therefore will not accurately describe the transitions for other types of molecules, such as linear polyatomics, which are not within the scope of this paper. The rotational energy levels of asymmetric tops can be described by the following three equations:

$$\bar{\nu}_P = \Delta E_i^{\mathrm{TOSH}} + \frac{1}{2}(A_1 + C_1)J(J+1) + \frac{1}{2}(A_1 - C_1)E_{\tau'} - \frac{1}{2}(A_0 + C_0)(J+1)(J+2) - \frac{1}{2}(A_0 - C_0)E_{\tau''}, \tag{18}$$

$$\bar{\nu}_Q = \Delta E_i^{\mathrm{TOSH}} + \frac{1}{2}(A_1 + C_1)J(J+1) + \frac{1}{2}(A_1 - C_1)E_{\tau'} - \frac{1}{2}(A_0 + C_0)J(J+1) - \frac{1}{2}(A_0 - C_0)E_{\tau''}, \tag{19}$$

$$\bar{\nu}_R = \Delta E_i^{\mathrm{TOSH}} + \frac{1}{2}(A_1 + C_1)(J+1)(J+2) + \frac{1}{2}(A_1 - C_1)E_{\tau'} - \frac{1}{2}(A_0 + C_0)J(J+1) - \frac{1}{2}(A_0 - C_0)E_{\tau''}. \tag{20}$$

As shown by these equations, for the frequency parameter we use the calculated anharmonic TOSH frequencies, $\Delta E_i^{\mathrm{TOSH}}$, which correspond to mode i. Frequencies calculated by any other means can be used instead if wanted. Additionally, in these equations we have A_1, B_1, C_1, which are the rotational constants for the upper vibrationally excited level, whereas A_0, B_0, C_0 are the rotational constants for the ground state. Although not immediately clear, the B rotational constant is present in these equations as it is used to calculate the value of E_τ.

We quickly notice the need to derive E_τ values for the upper and lower levels, shown as $E_{\tau'}$ and $E_{\tau''}$, respectively. These parameters describe a characteristic value of the sublevels, which are observed in the asymmetric rotor spectra as the usual equations to describe degeneracy (for other types of polyatomic molecules such as symmetric and spherical) are no longer an accurate representation of the energy levels (S. A. Cooke & P. Ohring 2013). The sublevel values are calculated using an asymmetry parameter, which depends on A, B, and C, therefore meaning the above Equations (18), (19), and (20) require all rotational constants. A typical energies diagram for an asymmetric molecule is shown in G. Herzberg (1945, Figure 17), which also shows its relation to the energy levels of a symmetric molecule.

Deriving the various sublevel energy values requires several steps: forming an energy matrix $\boldsymbol{E}(\kappa)$, diagonalizing, and then organizing the energies E_τ, from lowest to highest, to correspond correctly with the sublevels. Also consideration needs to be taken as to what axis orientation is used for the system, as this will change the order of constants used within the formation of the energy matrix. In the case of ozone, which is a near-prolate asymmetric top, we have selected the I^R format. I^R, specifically the I denotation, is mostly used when an asymmetric molecule is prolate-like in nature, and this parameter changes some of the values used in the calculation of the energy matrix. We will provide more implementation details in a forthcoming paper that describes the Pandora code, but the classic papers of G. W. King et al. (1943), G. Herzberg

(1945), and S. Golden (1948) contain an extensive description of the theory used.

Additional selection rules need to be applied depending on the symmetry of the sublevel and the molecule's overall nuclear spin. We used the rules specified by J. Flaud & R. Bacis (1998), which depend on the type of band a vibrational mode possesses, the parity of the sublevels, whether the isotopic variant is symmetric or asymmetric, and which oxygen isotopes are present. The excellent book by H. C. Allen & P. C. Cross (1963) goes into detail about the selection rules for the sublevels as a function of band type and has also been used to confirm the required selection rules for ozone. The vibration band type for each mode has been manually set within our work.

Once the possible transitions and their frequencies have been calculated for each mode, we now must produce a means to approximately model the intensities. Following T. M. Cross et al. (2022), we used a Boltzmann distribution with some modifications. The main modification is the adaptation of the energy component in the equation to now reflect the addition of E_τ and multiple rotational constants rather than just the solitary rotational constant B. The full equation we use is

$$\frac{n_J}{\sum n_J} = \frac{(2J+1)}{f} e^{-\left(\frac{\frac{1}{2}(A+C)J(J+1)+\frac{1}{2}(A-C)E_\tau}{kT}\right)}, \tag{21}$$

where n_J is the occupation of rotational level J, and f represents the rotational partition function. Once all of these components are calculated, we combine them to plot the spectrum. Given the usage of a Boltzmann distribution for our intensities, we have to make sure that the comparison spectrum is converted into the same arbitrary relative units rather than the typical atmospheric units that most databases use.

2.6. Computational Details

Two different potential energy surfaces (PES) for ozone are used within this work, one obtained from O. L. Polyansky et al. (2018) and the other from R. Dawes et al. (2013). The surfaces have been labeled with the abbreviations 18PoZo and 13DaLo, respectively, throughout this paper. We show that using two separate PES helps to illustrate how the anharmonic corrections are heavily reliant on the accuracy of the PES. Indeed, M. Spiegel et al. (2023) show that the vibrational frequencies of ozone are difficult to model using perturbation-based methods. They suggest that this could originate from the subtle electronic structure of the molecule. It is also worth noting the literature values from I. Gayday et al. (2020) that we use as comparison in Section 3.1 were obtained by the authors using the R. Dawes et al. (2013) potential.

The ozone equilibrium geometry was taken from the experimental data in T. J. Lee & G. E. Scuseria (1990) and O. Hino et al. (2006). These provide the bond angle, θ, as 116.°8 and the oxygen-to-oxygen bond length as 1.272 Å. The Born–Oppenheimer approximation leads us to the conclusion that the equilibrium geometry and the molecular potential function is the same for all isotopologs (P. Hennig & G. Strey 1976), so the same geometry from O. Hino et al. (2006) is used for all of the isotopic variants of ozone within this paper.

The diagonal elements of the Cartesian Hessian matrix in Equation (6) are computed using

$$\eta_{ii} = \frac{1}{12h^2}(-E_{(-2,0)} + 16E_{(-1,0)} - 30E_{(0,0)} + 16E_{(1,0)} - E_{(2,0)}). \tag{22}$$

Whereas the nondiagonal elements are described as

$$\eta_{ij} = \frac{1}{4h^2}(E_{(-1,-1)} - E_{(-1,1)} - E_{(1,-1)} + E_{(1,1)}). \tag{23}$$

The constant h represents the step taken to displace the specific atoms—in our work we arbitrarily selected a value of 0.005 Bohrs (atomic units)—from the stable range of values reported in P.-O. Åstrand et al. (2000). The $E_{(a,b)}$ describes the energy calculated at a nuclear configuration displaced by $ah + bh$ from equilibrium.

The cubic and quartic constants required to calculate the TOSH anharmonically corrected band origin (Equation (10)) are obtained through a method similar to the second-order derivatives for the Cartesian Hessian.

The cubic diagonal elements are computed via the following equation:

$$\eta_{iii} = \frac{1}{2h_i^3}(-E_{(-2,0)} + 2E_{(-1,0)} - 2E_{(1,0)} + E_{(2,0)}). \tag{24}$$

The cubic nondiagonal elements are expressed as

$$\eta_{iij} = \frac{1}{2h_i^2 h_j}(-E_{(-1,-1)} + E_{(-1,1)} + 2E_{(0,-1)} - 2E_{(0,1)} - E_{(1,-1)} + E_{(1,1)}). \tag{25}$$

The quartic diagonal elements are calculated using

$$\eta_{iiii} = \frac{1}{h_i^4}(E_{(-2,0)} - 4E_{(-1,0)} + 6E_{(0,0)} - 4E_{(1,0)} + E_{(2,0)}). \tag{26}$$

Finally, the quartic nondiagonal elements are

$$\eta_{iijj} = \frac{1}{h_i^2 h_j^2}(E_{(-1,-1)} - 2E_{(-1,0)} + E_{(-1,1)} - 2E_{(0,-1)} + 4E_{(0,0)} - 2E_{(0,1)} + E_{(1,-1)} - 2E_{(1,0)} + E_{(1,1)}), \tag{27}$$

where $h_i = h/\sqrt{\omega}_i$ and $h_j = h/\sqrt{\omega}_j$ are the adaptive steps along the Q_i and Q_j normal coordinates (A. Erba et al. 2019). The inclusion of adaptive steps, which depend on the normal coordinates, is a slight modification from the theory of C. Y. Lin et al. (2008). For cubic and quantic constant calculations, the $E_{(a,b)}$ within Equations (24)–(27) represent the energy calculated at a nuclear configuration displaced by $ah_iQ_i + bh_jQ_j$ from equilibrium. These constants are then stored as a compressed matrix.

3. Results and Discussion: Spectroscopic Constants

First, in Section 3.1, we compare the spectroscopic constants from the literature and those calculated by Epimetheus using two different potentials, one from R. Dawes et al. (2013) and one from O. L. Polyansky et al. (2018).

Following this, Section 3.2 shows how our calculated band origins compare with the rest of the isotopic variants of ozone. This includes the ozone isotopologs 678, 786, 768, 677, 767, 788, 878, 778, and 787. Only the band origins have been

Table 2
Constants for Ozone 666 ($^{16}O_3$) and Ozone 668 ($^{16}O^{16}O^{18}O$), All Given in Wavenumbers (cm^{-1})

Mode	Constant	666 ($^{16}O_3$)†					668 ($^{16}O^{16}O^{18}O$)†				
		Lit.	Epimetheus				Target	Epimetheus			
		98FlBa	18PoZo	ΔLit.	13DaLo	ΔLit.	20GaTe	18PoZo	ΔLit.	13DaLo	ΔLit
000	*A*	3.554	3.557	−0.003	3.557	−0.003	3.488$^{\gamma}$	3.491	+0.003	3.491	+0.003
	B	0.445	0.449	+0.004	0.449	+0.004	0.420$^{\gamma}$	0.424	+0.004	0.424	+0.004
	C	0.395	0.399	+0.004	0.399	+0.004	0.374$^{\gamma}$	0.378	+0.004	0.378	+0.004
100	ω_1	1134.9$^{\beta}$	1134.9	⋯	1122.4	−12.5	⋯	1122	⋯	1112	⋯
	ν_1	1103.1	1121.7	+18.6	1101.7	−1.4	1090$^{\alpha}$	1101	+11	1083.2	−6.8
	A	3.557	3.511	−0.046	3.512	−0.045	3.498	3.479	−0.019	3.311	−0.187
	B	0.443	0.442	−0.001	0.442	−0.001	0.418	0.419	+0.001	0.423	+0.005
	C	0.393	0.393	0.0	0.393	0.0	0.376	0.374	−0.002	0.375	−0.001
010	ω_2	716.0$^{\beta}$	715.5	−0.5	708.7	−7.3	⋯	698.7	⋯	692.2	⋯
	ν_2	700.9	702.4	+1.5	690.8	−10.1	684.6$^{\alpha}$	686.2	+1.6	675.7	−8.9
	A	3.607	3.530	−0.077	3.530	−0.077	3.549	3.490	−0.059	3.653	+0.096
	B	0.444	0.444	0.0	0.443	−0.001	0.419	0.419	0.0	0.423	+0.004
	C	0.392	0.394	+0.002	0.394	+0.002	0.372	0.374	+0.002	0.379	+0.007
001	ω_3	1089.2$^{\beta}$	1090.0	+0.8	1089.6	+0.4	⋯	1073	⋯	1071	⋯
	ν_3	1042.1	1046.9	+4.8	1039.0	−3.1	1028$^{\alpha}$	1032	+4	1027	+1
	A	3.501	3.557	+0.056	3.557	+0.056	3.451	3.462	+0.011	3.442	−0.009
	B	0.441	0.449	+0.008	0.449	+0.008	0.416	0.424	+0.008	0.424	+0.008
	C	0.391	0.399	+0.008	0.399	+0.008	0.366	0.378	+0.012	0.378	+0.012

Note. 98FlBa refers to J. Flaud & R. Bacis (1998), which is also designated by α, 20GaTe refers to I. Gayday et al. (2020), 18PoZo refers to O. L. Polyansky et al. (2018), and 13DaPh refers to R. Dawes et al. (2013). A γ next to a value indicates the constant has been taken from experimental data reported in G. D. Carney et al. (1978). A β next to a value indicates the constant has been taken from A. Barbe et al. (1974). A † next to entries indicates that there are spectra available for comparison from HITRAN. The constant ω refers to the harmonic frequency of the mode, whereas ν refers to the anharmonically corrected frequency.

assessed for those as little data exist for rotational constants, presumably due to the low abundances of those isotopologs.

We will now briefly discuss the comparative data sources, which are denoted by the column "Lit." in the following tables. J. Flaud & R. Bacis (1998, abbreviated to 98FlBa) is an empirical study reporting spectroscopic constants of experiment quality. These data are either represented by the column header "98FlBa" or α (when values are used in combination with a different column header). A. Barbe et al. (1974) is an experimental study and has been used to provide the harmonic frequencies for some of the isotopologs such as 666 and 888, and whose values are indicated by a β in the following tables.

The data from I. Gayday et al. (2020, abbreviated to 20GaTe) are not of experimental quality but instead is accurate theory. Some of the constants reported in this study, specifically all ground-state rotational constants and band origins, are in fact experimental results from G. D. Carney et al. (1978) and J. Flaud & R. Bacis (1998), respectively. They have been selected rather than 20GaTe's constants due to their experiment quality. The G. D. Carney et al. (1978) entries are highlighted by the mathematical symbol γ in the following tables. All other I. Gayday et al. (2020) constants (excited-state rotational constants) are obtained from the supplementary material and come from rotational fitting.

Finally, we have B. C. Hathorn & R. A. Marcus (2001, abbreviated to 01HaMa), to provide the band origins for each vibrational mode. The data here are obtained using an approximate method based on a different ab initio level of theory; however, this was deemed an appropriate level of theory as the focus of this study is less on the remaining isotopologs due to their scarcity or prominence in astronomy. Therefore, the data here are included simply to provide an approximate benchmark, as well as show the breadth of Epimetheus and its ease at modeling isotopologs. As these data are not of experimental or highly accurate theory, it serves simply as a general indication of our capabilities, and the accuracy between Epimetheus and this data set has less importance than against experimental or accurate theory.

3.1. Comparisons of Band Origins and Rotational Constants

Table 2 displays the spectroscopic constants for ozone 666 ($^{16}O_3$) and 668 ($^{16}O^{16}O^{18}O$). Note that the table columns for each isotopic variant are organized as follows, from left to right: the literature value (typically from either J. Flaud & R. Bacis 1998 or I. Gayday et al. 2020) followed by the value from the O. L. Polyansky et al. (2018) potential and its difference to the literature values, and finally the value from the R. Dawes et al. (2013) potential and its difference to the literature values. The rows are organized as follows: we first cover the ground or "000" state, starting with the *A* rotational constant then the *B* and *C* constants. The same pattern is then repeated with the "100," "010," and "001" states, with the exception of the harmonic frequency, ω_i, and the anharmonic frequency, ν_i, values preceding the rotational constants. Where no data are present, it has been indicated by a − character.

A key point to note here is that these isotopologs are symmetric and asymmetric versions of ozone, respectively, and therefore correspond to different point symmetry groups. This is a factor that will become more important further into the discussion.

First, focusing on the rotational constants for 666 (Table 2), we see that there is little variation in the results obtained between the two potentials. Thus, we mainly highlight the

comparisons to the literature, which pertain to both of the Epimetheus results. Overall, typically the obtained rotational constants are consistent with the literature well within 3%. In particular, the B and C rotational constants are usually reproduced within a $\pm 0.002\,\mathrm{cm}^{-1}$ difference to the literature. The A rotational constant shows a difference from the literature ranging from 0.045 to $0.077\,\mathrm{cm}^{-1}$. As the A rotational constant is an order of magnitude larger than B and C, and if the method has a similar accuracy for each rotational constant, one would expect the difference from literature values for A to also be roughly a magnitude larger also. This appears to be the case in our results. In some scenarios, such as for the bending mode of 666, the deviation of the A constant from the literature values is $0.077\,\mathrm{cm}^{-1}$, which differs by roughly a magnitude from the deviation on the C constant, which has a difference of $0.002\,\mathrm{cm}^{-1}$.

If we now consider the constants for 668 (Table 2), unlike with 666, by using different potentials we find a significant impact on the obtained rotational constants, with the 18PoZo potential typically providing more accurate results. For example, for a rotational constant A of mode 100, 18PoZo gives a difference of $-0.019\,\mathrm{cm}^{-1}$, whereas 13DaLo has a difference of $-0.187\,\mathrm{cm}^{-1}$. This is nearly an order of magnitude different and quite a large discrepancy from the literature (I. Gayday et al. 2020). Potentially, this is due to the refinement of the potential, as it is more recent than 13DaLo, and therefore may have utilized better methodologies in its creation.

Since the harmonic frequencies, indicated by the entries for ω_i (rather than just the anharmonic frequencies, ν_i), are also available in the literature, we can also use them to verify the accuracy of our method and/or the PES. Let us consider here the vibrational frequencies for 666. We can see that by using 18PoZo Epimetheus reproduces the harmonic frequencies within a single wavenumber of the benchmark values from O. Hino et al. (2006). This is not the case for 13DaLo: We can indeed reproduce the mode 001 harmonic value within a wavenumber, but are unable to replicate this accuracy for both 100 and 010 modes, with differences of $-12.6\,\mathrm{cm}^{-1}$ and $-7.3\,\mathrm{cm}^{-1}$, respectively.

The comparisons become more complicated if we consider the anharmonic frequencies, ν_i. When using 18PoZo we no longer have a general trend of high accuracy, but instead a variation depending on the mode. For example, for mode 010 (which is the best result) we only have a discrepancy of $+1.5\,\mathrm{cm}^{-1}$. On the other hand, for mode 100 we obtain a difference of $+18.6\,\mathrm{cm}^{-1}$. Interestingly, by using 18PoZo for 666 all ν_i values have a positive difference from J. Flaud & R. Bacis (1998). This would suggest that our derived anharmonic corrections are smaller than they should be, since the harmonic values for that potential reproduce the literature values very closely. This is an issue that could potentially be reduced within Epimetheus if other methods for calculating the cubic and quartic constants are used.

With 13DaLo we instead obtain inverse results compared to 18PoZo: Mode 100 is the best result, with a difference of $-1.4\,\mathrm{cm}^{-1}$, while mode 010 is the worst, with $-10.1\,\mathrm{cm}^{-1}$. In general, it appears that all the ν_i values for 13DaLo are overcorrected, potentially arising from the fact that the harmonic frequencies are mostly underestimated for this PES.

Finally, the vibrational frequencies for 668 exhibit similar correction patterns to 666, i.e., 18PoZo typically undercorrects the frequencies and leads to positive differences, whereas 13DaLo overcorrects causing negative differences. The main difference between 666 and 668 is the size of the corrections for the various modes. For example, for mode 100, 666 has ν_1 deviating by $+18.6\,\mathrm{cm}^{-1}$ (18PoZo) and $-1.4\,\mathrm{cm}^{-1}$ (13DaLo), whereas 668 deviates by $+11\,\mathrm{cm}^{-1}$ (18PoZo) and $-6.8\,\mathrm{cm}^{-1}$ (13DaLo) for the same mode. In contrast, the predictions for modes 010 and 001 are of similar quality for both 666 and 668.

The spectroscopic constants for ozone 686 ($^{16}O^{18}O^{16}O$) and 667 ($^{16}O^{16}O^{17}O$) are shown in Table 3. Similar to 666 and 668 in Table 2, they are, respectively, symmetric and asymmetric isotopologs of ozone, and therefore they correspond to different point symmetry groups.

Focusing first on the rotational constants, we see a similar pattern as before. The rotational constants for the symmetric isotopolog 686 are mostly the same for the two potentials and are good approximations of the literature. This is not the case with the asymmetric 667 isotopolog, whose values vary more than 686's. Overall, for 667 it appears that 18PoZo reproduces the target literature values with this PES better than 18PoZo. For example, the rotational constants for mode 001 obtained with 18PoZo differ from the literature by $-0.091\,\mathrm{cm}^{-1}$, $-0.001\,\mathrm{cm}^{-1}$, and $+0.001\,\mathrm{cm}^{-1}$, for A, B, and C, respectively, while 13DaLo gives differences of $+0.102\,\mathrm{cm}^{-1}$, $+0.004\,\mathrm{cm}^{-1}$, and $+0.007\,\mathrm{cm}^{-1}$.

The 18PoZo PES for 686 produces anharmonic frequencies that deviate in a similar manner to those of 666. This is characterized mainly by the larger difference for mode 100 in the region of $18\,\mathrm{cm}^{-1}$, then an extremely accurate result for mode 010 of less than $2\,\mathrm{cm}^{-1}$, followed by a value roughly $5\,\mathrm{cm}^{-1}$ off the literature values for mode 001. When using 13DaLo PES for 686, the results are similar to 666: With modes 100 and 001, we obtain good results, less than a couple of wavenumbers off, with a deterioration in accuracy for mode 010.

Table 4 shows the spectroscopic constants for the ozone isotopologs 676 ($^{16}O^{17}O^{16}O$) and 668 ($^{16}O^{18}O^{18}O$). For 688, modes 100 and 001 have no reported data for their rotational constants. Similar to the previous Tables 2–3, we have a symmetric specie (676) and an asymmetric specie (688) of ozone. The results for 676 and 688 are very similar to what has been shown before. The only significant novelty now is that for 676 all fundamental frequencies are seemingly overestimated if 18PoZo is used, or seemingly underestimated in case 13DaLo is implemented. The overall accuracy for each potential depends on the mode however.

Table 5 shows the constants for 868 ($^{18}O^{16}O^{18}O$) and 888 ($^{18}O_3$). For 888, we have the harmonic literature values from A. Barbe et al. (1974), allowing us a further insight into the abilities of the anharmonic corrections of the method. In particular, we show again an excellent agreement for harmonic frequencies when using the 18PoZo PES, while the results using the 13DaLo PES are not as good. Notice that Table 5 only contains symmetric isotopologs, and this is reflected in the results we obtain. No further discussion will be included here as these isotopologs match the patterns and general trends previously discussed for the other symmetric isotopologs (676, 686, and 666).

Finally, in Table 6 we compare the results for ozone 777 ($^{17}O_3$). No data, frequencies, or rotational constants are available for the 010 mode of 777. We also have no harmonic frequencies, which means we cannot evaluate how accurate the initial Hessian calculations are. Based on the data available for

Table 3
Constants for Ozone 686 ($^{16}O^{18}O^{16}O$) and Ozone 667 ($^{16}O^{16}O^{17}O$), All Given in Wavenumbers (cm^{-1})

Mode	Constant	686 ($^{16}O^{18}O^{16}O$)†					667 ($^{16}O^{16}O^{17}O$)†				
		Lit.	Epimetheus				Lit.	Epimetheus			
		20GaTe	18PoZo	ΔLit.	13DaLo	ΔLit.	98FlBa	18PoZo	ΔLit.	13DaLo	ΔLit
000	A	3.290[γ]	3.293	+0.003	3.293	+0.003	3.519	3.522	+0.003	3.522	+0.003
	B	0.445[γ]	0.449	+0.004	0.449	+0.004	0.432	0.436	+0.004	0.436	+0.004
	C	0.391[γ]	0.395	+0.004	0.395	+0.004	0.384	0.388	+0.004	0.388	+0.004
100	ω_1	…	1105	…	1093	…	…	1127.3	…	1115.4	…
	ν_1	1074[α]	1092	+18	1073	−1	1095.7	1111.4	+15.7	1091.7	−4.0
	A	3.299	3.256	−0.043	3.256	−0.043	3.522	3.452	−0.070	3.346	−0.176
	B	0.443	0.442	−0.001	0.442	−0.001	0.430	0.429	−0.001	0.436	+0.006
	C	0.393	0.389	−0.004	0.389	−0.004	0.382	0.381	−0.001	0.386	+0.004
010	ω_2	…	707.1	…	700.3	…	…	706.8	…	700.1	…
	ν_2	696.3[α]	694.5	−1.8	683.2	−13.1	692.4	694.0	+1.6	682.8	−9.6
	A	3.351	3.276	−0.075	3.275	−0.076	3.570	3.479	−0.091	3.672	+0.102
	B	0.444	0.444	0.0	0.443	−0.001	0.431	0.430	−0.001	0.435	+0.004
	C	0.389	0.391	+0.002	0.391	+0.002	0.382	0.383	+0.001	0.389	+0.007
001	ω_3	…	1053	…	1053	…	…	1082.2	…	1081.3	…
	ν_3	1008[α]	1013	+5	1006	−2	1035.4	1040.0	+4.6	1033.4	−6.6
	A	3.253	3.293	+0.040	3.293	+0.040	3.467	3.527	+0.060	3.499	+0.032
	B	0.441	0.449	+0.008	0.449	+0.008	0.428	0.435	+0.007	0.436	+0.008
	C	0.384	0.395	+0.011	0.395	+0.008	0.380	0.387	+0.007	0.388	+0.008

Note. 98FlBa refers to J. Flaud & R. Bacis (1998), which is also designated by α, 20GaTe refers to I. Gayday et al. (2020), 18PoZo refers to O. L. Polyansky et al. (2018), and 13DaPh refers to R. Dawes et al. (2013). A γ next to a value indicates the constant has been taken from experimental data reported in G. D. Carney et al. (1978). A † next to entries indicates that there are spectra available for comparison from HITRAN. The constant ω refers to the harmonic frequency of the mode, whereas ν refers to the anharmonically corrected frequency.

Table 4
Constants for Ozone 676 ($^{16}O^{17}O^{16}O$) and Ozone 688 ($^{16}O^{18}O^{18}O$), All Given in Wavenumbers (cm^{-1})

Mode	Constant	676 ($^{16}O^{17}O^{16}O$)†					688 ($^{16}O^{18}O^{18}O$)				
		Lit.	Epimetheus				Lit.	Epimetheus			
		98FlBa	18PoZo	ΔLit.	13DaLo	ΔLit.	98FlBa	18PoZo	ΔLit.	13DaLo	ΔLit
000	A	3.414	3.417	+0.003	3.417	+0.003	3.225	3.227	+0.002	3.227	+0.002
	B	0.445	0.449	+0.004	0.449	+0.004	0.420	0.423	+0.003	0.423	+0.003
	C	0.393	0.397	+0.004	0.397	+0.004	0.371	0.374	+0.003	0.374	+0.003
100	ω_1	…	1118.9	…	1106.8	…	…	1091.6	…	1080.9	…
	ν_1	1087.8	1106.2	+18.4	1086.6	−1.2	1060.7	1072.2	+11.5	1055.0	−5.7
	A	3.415	3.376	−0.039	3.377	−0.038	…	3.159	…	3.065	…
	B	0.443	0.442	−0.001	0.442	−0.001	…	0.416	…	0.423	…
	C	0.391	0.391	0.0	0.391	0.0	…	0.368	…	0.372	…
010	ω_2	…	711.2	…	704.4	…	…	690.9	…	684.3	…
	ν_2	697.1	698.4	+1.3	686.9	−10.2	677.5	678.7	+1.2	668.4	−9.1
	A	3.466	3.395	−0.071	3.395	−0.071	3.273	3.190	−0.083	3.357	+0.084
	B	0.444	0.444	0.0	0.444	0.0	0.419	0.418	−0.001	0.423	+0.004
	C	0.391	0.393	+0.002	0.392	+0.001	0.369	0.370	+0.001	0.376	+0.007
001	ω_3	…	1070.8	…	1070.4	…	…	1036.3	…	1034.9	…
	ν_3	1024.4	1029.1	+4.7	1021.6	−2.8	993.9	998.2	+4.3	993.1	−0.8
	A	3.364	3.417	+0.053	3.417	+0.053	…	3.230	…	3.189	…
	B	0.441	0.449	+0.008	0.449	+0.008	…	0.422	…	0.424	…
	C	0.390	0.397	+0.007	0.397	+0.007	…	0.373	…	0.374	…

Note. 98FlBa refers to J. Flaud & R. Bacis (1998), 18PoZo refers to O. L. Polyansky et al. (2018), and 13DaPh refers to R. Dawes et al. (2013). A † next to entries indicates that there are spectra available for comparison from HITRAN. The constant ω is the harmonic frequency of the mode, whereas ν is the anharmonically corrected frequency. The column title "Lit." naturally indicates the literature source of the target values.

Table 5
Constants for Ozone 868 ($^{18}O^{16}O^{18}O$) and Ozone 888 ($^{18}O_3$), All Given in Wavenumbers (cm^{-1})

Mode	Constant	868 ($^{18}O^{16}O^{18}O$)‡					888 ($^{18}O_3$)‡				
		Lit.	Epimetheus				Lit.	Epimetheus			
		20GaTe	18PoZo	ΔLit.	13DaLo	ΔLit.	98FlBa	18PoZo	ΔLit.	13DaLo	ΔLit
000	*A*	3.422[γ]	3.427	+0.005	3.427	+0.005	3.158	3.161	+0.003	3.161	+0.003
	B	0.396[γ]	0.399	+0.003	0.399	+0.003	0.396	0.399	+0.003	0.399	+0.003
	C	0.354[γ]	0.357	+0.003	0.357	+0.003	0.351	0.354	+0.003	0.354	+0.003
100	ω_1	⋯	1102	⋯	1089	⋯	1070.0[β]	1069.8	−0.2	1058.1	−11.9
	ν_1	1072[α]	1089	+17	1070	−2	1041.6	1058.1	+16.5	1039.6	−2
	A	3.438	3.376	−0.062	3.377	−0.061	3.161	3.122	−0.039	3.123	−0.038
	B	0.394	0.394	0.0	0.393	−0.001	0.394	0.393	−0.001	0.393	−0.001
	C	0.357	0.352	−0.005	0.352	−0.005	0.349	0.349	0.0	0.349	0.0
010	ω_2	⋯	681.8	⋯	675.4	⋯	674.8[β]	674.5	−0.3	668.1	−6.7
	ν_2	668.1[α]	669.8	+1.7	658.4	−9.7	661.5	662.9	+1.2	651.8	−11.1
	A	3.479	3.391	−0.088	3.391	−0.088	3.203	3.138	−0.065	3.138	−0.065
	B	0.395	0.394	−0.001	0.394	−0.001	0.395	0.395	0.0	0.394	−0.001
	C	0.352	0.353	+0.001	0.353	+0.001	0.349	0.351	+0.002	0.350	+0.001
001	ω_3	⋯	1065	⋯	1065	⋯	1026.5[β]	1027.5	+1.0	1027.2	+0.7
	ν_3	1019[α]	1024	+5	1016	−3	984.8	989.1	+4.3	982.3	−2.5
	A	3.381	3.425	+0.044	3.425	+0.044	3.114	3.161	+0.047	3.161	+0.047
	B	0.392	0.399	+0.007	0.399	+0.007	0.393	0.399	+0.006	0.399	+0.006
	C	0.345	0.357	+0.012	0.357	+0.012	0.348	0.354	+0.006	0.354	+0.006

Note. 98FlBa refers to J. Flaud & R. Bacis (1998), which is also designated by α, 20GaTe refers to I. Gayday et al. (2020), 18PoZo refers to O. L. Polyansky et al. (2018), and 13DaPh refers to R. Dawes et al. (2013). A γ next to a value indicates the constant has been taken from experimental data reported in G. D. Carney et al. (1978). A β next to a value indicates the constant has been taken from A. Barbe et al. (1974). The constant ω is the harmonic frequency of the mode, whereas ν is the anharmonically corrected frequency. The column title "Lit." naturally indicates the literature source of the target values. A ‡ indicates that comparison data from S&MPO Y. L. Babikov et al. (2014) were available.

Table 6
Constants for Ozone 777 ($^{17}O_3$), All Given in Wavenumbers (cm^{-1})

Mode	Constant	777 ($^{17}O_3$)				
		Lit.	Epimetheus			
		98FlBa	18PoZo	ΔLit.	13DaLo	ΔLit.
000	*A*	3.344	3.347	+0.003	3.347	+0.003
	B	0.419	0.423	+0.004	0.423	+0.004
	C	0.372	0.375	+0.003	0.375	+0.003
100	ω_1	⋯	1100.8	⋯	1088.8	⋯
	ν_1	1070.9	1088.5	+17.6	1069.3	−1.6
	A	3.347	3.304	−0.043	3.306	−0.041
	B	0.417	0.416	−0.001	0.416	−0.001
	C	0.369	0.370	+0.001	0.370	+0.001
010	ω_2	⋯	694.0	⋯	687.5	⋯
	ν_2	⋯	681.7	⋯	670.4	⋯
	A	⋯	3.322	⋯	3.322	⋯
	B	⋯	0.418	⋯	0.417	⋯
	C	⋯	0.371	⋯	0.371	⋯
001	ω_3	⋯	1057.3	⋯	1056.9	⋯
	ν_3	1012.2	1016.7	+4.5	1009.4	−2.8
	A	3.296	3.347	+0.051	3.347	+0.051
	B	0.415	0.423	+0.008	0.423	+0.008
	C	0.368	0.375	+0.007	0.375	+0.007

Note. 98FlBa refers to J. Flaud & R. Bacis (1998), 18PoZo refers to O. L. Polyansky et al. (2018), and 13DaPh refers to R. Dawes et al. (2013). The constant ω is the harmonic frequency of the mode, whereas ν is the anharmonically corrected frequency. The column title "Lit." naturally indicates the literature source of the target values.

all other modes and the harmonic rotational constants, the results in Table 6 are consistent with the previous analysis.

As 777 is a symmetric variant, there is little difference in the rotational constants when using the two potentials. The frequency for 100 performs as expected, following the pattern seen for the other symmetric isotopologs: A discrepancy nearing $+20\,cm^{-1}$ is obtained for 18PoZo, and a result only a couple of wavenumbers off for 13DaLo. The asymmetric stretch mode 001 results are what we also expect as they are not too dissimilar, being within $5\,cm^{-1}$ for both (but over for 18PoZo and under for 13DaLo).

3.2. Other Isotopic Variants Band Origins

In this section, our results are compared with B. C. Hathorn & R. A. Marcus (2001). Table 7 shows the remaining species in descending order of abundance. For these isotopomers all the data for each mode's band origin are available.

In general, the accuracy for each mode differs depending on the potential used, with reoccurring patterns similar to what we have seen in Section 3.1. The 18PoZo or 13DaLo potentials present results that vary in accuracy depending on the mode and the symmetry of the isotopologs. For example, Mode 100 (ν_1) for 18PoZo has discrepancies of up to $20\,cm^{-1}$ difference, with the asymmetric variants typically having a difference of less than $15\,cm^{-1}$. This is in contrast to 13DaLo's mode 100 (ν_1), whose differences from the literature lie between 1 and $4.1\,cm^{-1}$ and have an indistinct pattern in accuracy depending on the symmetry of the isotopolog.

Concerning the ν_2 mode, we see for 18PoZo the differences range from $1.1\,cm^{-1}$ to $1.8\,cm^{-1}$. Conversely, 13DaLo

Table 7
Band Origins for the Remaining Isotopologs of Ozone

Isotopomer	Mode	Literature 01HaMa	Epimetheus			
			18PoZo	ΔLit.	13DaLo	ΔLit.
678 ($^{16}O^{17}O^{18}O$)	100	1071.9	1085.8	+13.9	1068.3	−3.6
	010	681.3	682.4	+1.1	672.0	−9.3
	001	1012.9	1014.5	+1.6	1009.3	−3.6
786 ($^{17}O^{18}O^{16}O$)	100	1065.4	1082.1	+16.7	1063.4	−2.0
	010	685.2	686.3	+1.1	675.3	−9.9
	001	1001.9	1005.9	+4.0	999.6	−2.3
768 ($^{17}O^{16}O^{18}O$)	100	1079.8	1095.2	+15.4	1075.7	−4.1
	010	676.1	677.7	+1.6	666.6	−9.5
	001	1025.1	1028.7	+3.6	1022.3	−2.8
677 ($^{16}O^{17}O^{17}O$)	100	1079.6	1095.8	+16.2	1076.7	−2.9
	010	688.9	690.1	+1.2	679.0	−9.9
	001	1018.6	1022.1	+3.5	1015.6	−3.0
767 ($^{17}O^{16}O^{17}O$)	100	1087.2	1104.5	+17.3	1084.8	−2.4
	010	684.0	685.5	+1.5	674.0	−10.0
	001	1030.7	1034.7	+4.0	1027.1	−3.6
788 ($^{17}O^{18}O^{18}O$)	100	1048.7	1065.0	+16.3	1046.5	−2.2
	010	669.0	670.5	+1.5	659.6	−9.4
	001	989.5	994.1	+4.6	988.0	−1.5
878 ($^{18}O^{17}O^{18}O$)	100	1055.6	1072.8	+17.2	1053.8	−1.6
	010	664.5	666.3	+1.8	655.1	−9.4
	001	1000.6	1005.6	+5.0	998.4	−2.2
778 ($^{17}O^{17}O^{18}O$)	100	1063.3	1079.2	+15.9	1060.2	−3.1
	010	672.5	674.0	+1.5	663.1	−9.4
	001	1006.4	1010.5	+4.1	1004.2	−2.2
787 ($^{17}O^{18}O^{17}O$)	100	1056.5	1074.2	+17.7	1055.5	−1.0
	010	676.7	678.1	+1.4	666.9	−9.8
	001	995.4	1000.4	+5.0	993.5	−1.9

Note. These are organized in order of decreasing abundance, and all results have been presented in units of wavenumbers (cm^{-1}). 01HaMa refers to B. C. Hathorn & R. A. Marcus (2001), 18PoZo to O. L. Polyansky et al. (2018), and 13DaLo to R. Dawes et al. (2013).

provides results that range from 9.3 cm^{-1} to 10.0 cm^{-1}. Interestingly, both potentials provide results that have roughly a constant difference across all isotopologs, which suggests the code provides a consistent correction of this particular mode.

In general, the differences between the accurate literature data and our results for ozone are mostly driven by the nature of the anharmonic corrections, instead of by the specific potential implemented. Indeed, the approach we have chosen is a simplification of VPT2 and truncates the energy expansion equation (see TOSH Equations (21)–(24) in C. Y. Lin et al. 2008) used to derive our shift parameter σ. More specifically, some of the cubic constants (see Equations (24) and (25)) that are traditionally included in the VPT2 method are not calculated or used within the TOSH framework. We think it likely that the missing constants could have a noticeable contribution to the correction, and thus lead to the inaccuracies in our approach. This issue presumably will only affect molecules of high symmetry, the reasons for which are discussed later in this section. These hypotheses are not tested within this paper, as the focus is on simply seeing the performance of the method, and from these results the methodology will be tested then modified accordingly.

For example, the effect of neglecting some VPT2 constants is striking for the results obtained with the 18PoZo potential: The harmonic values for this potential accurately reproduce the experimental data, yet the anharmonic corrections computed are too small to fully account for the observed anharmonicity. Conversely, the 13DaLo potential leads to better corrected values because the harmonic frequencies are underestimated initially. The limited anharmonic correction computed with our truncated approach has therefore less of a frequency gap to correct for.

Table 8 shows the frequencies, both harmonic and anharmonic, that are produced by either PES in Epimetheus and the experimental literature values. The main aim of this table is to explore how the two PES predict the actual anharmonic shift, and how it then compares to the actual anharmonic shift that is observed.

For both potentials the 100 mode correction is substantially underestimated. The simulations using 13DaLo manage to recover about two-thirds of the correction, whereas with 18PoZo we only recover about half of what was expected. For the 010 mode, the magnitude of the correction is consistent with the literature. For example, for ozone 666 we would expect a correction of 15.1 cm^{-1}; 18PoZo gives a correction of 13.1 cm^{-1}, while 13DaLo gives a correction of 17.9 cm^{-1}, meaning both are only a couple of wavenumbers off. We notice from this example that 18PoZo is undercorrecting and 13DaLo is overcorrecting, something which is also true for the 010

Table 8
For Ozone 666 and 888, a Comparison between the Harmonic and Anharmonic Values from Epimetheus is Shown for Each Mode and Each Potential

Source	Mode	666 ($^{16}O_3$)			888 ($^{18}O_3$)		
		Harmonic	Anharmonic	Δ	Harm	Anharmonic	Δ
Exp. (98FlBa)	100	1134.9⋆	1103.1	−31.8	1070.0⋆	1041.6	−28.4
	010	716.0⋆	700.9	−15.1	674.8⋆	661.5	−13.3
	001	1089.2⋆	1042.1	−47.1	1026.5⋆	984.8	−41.7
18PoZo	100	1134.9	1121.7	−13.2	1069.8	1058.1	−11.7
	010	715.5	702.4	−13.1	674.5	662.9	−11.6
	001	1090.0	1046.9	−43.1	1027.5	989.1	−38.4
13DaLo	100	1121.4	1101.7	−19.7	1058.1	1039.6	−18.5
	010	708.7	690.8	−17.9	668.1	651.8	−16.3
	001	1089.6	1039.0	−50.6	1027.2	982.3	−44.9

Note. All results have been presented in units of wavenumbers (cm^{-1}). 18PoZo refers to O. L. Polyansky et al. (2018) and 13DaPh refers to R. Dawes et al. (2013). Exp. 98FlBa represents the difference between the harmonic and anharmonic value from the literature by J. Flaud & R. Bacis (1998). A ⋆ next to a value indicates the constant has been taken from A. Barbe et al. (1974).

mode for 888; 18PoZo has a $-1.7\,cm^{-1}$ difference to the target value, and 13DaLo is then $+3\,cm^{-1}$. Moving onto the asymmetric 001 mode, for 666 once again both potentials give results within approximately 4 wavenumbers. Like before, with mode 010, 18PoZo underestimates the correction, whereas 13DaLo overestimates; the same is also true for ozone 888. The trend emerging here may not be the case for all types of isotopomers. We only have a small sample of anharmonic corrections to compare with, and only for the symmetric variants of ozone.

The mode 100, which is the designation given to the symmetric stretch, shows the largest correction. The corrections rely heavily upon the calculations of the cubic constants, which gives rise to the shift parameter σ, and to a lesser degree the quartic. In particular, the cubic constants Equations (24) and (25) are symmetric in terms of the shift displacements. This numerical approach is well adapted to symmetric modes as the various energy contributions computed along those modes will not cancel out. However, displacements along the asymmetric mode (mode 001) can lead to near-perfect cancellation of all terms for symmetric isotopomers and potentially cancel completely its anharmonic contribution. Ironically, this contribution is what is required to correct the frequencies of the symmetric modes 100 and 010, thus leading to errors for their anharmonic frequencies. Meanwhile, the asymmetric mode is corrected by contributions coming from the symmetric modes that are correctly calculated. We can observe this in the results from Table 8: For either potential (18PoZo or 13DaLo), the correction for the symmetric stretch 100 is lower than expected, as it is composed of the correction due to its interaction with the (symmetric) bending mode 010 and the asymmetric stretch mode 001, which we presume to be nearly zero. The 010 bending mode is corrected by nearly the same amount, since it shares its anharmonic correction with the symmetric stretch mode (100). It is likely that its interaction with the asymmetric stretch (001) is also near zero for the reasons stated above. The asymmetric stretch (001) is instead fully corrected by its interactions with both symmetric modes.

In the case of an asymmetric molecule, we postulate that more terms survive in the calculation of the cubic and quartic constants with this new intrinsic asymmetry. This would explain why the results for mode 100 in the case of asymmetric ozone variants are typically better, although not as good as we would expect if this is the sole reason for the poor approximations of the anharmonic corrections. In Table 7, we see that when an asymmetric variant is present, the difference between the literature and our calculations is reduced down to a couple of wavenumbers for the symmetric mode. For example, 787 has a difference of $17.7\,cm^{-1}$, and 778 has a difference of $15.9\,cm^{-1}$. It is difficult to get a more precise assessment of the sources of discrepancy, as the harmonic values are not available in the literature for all isotopomers. With this information, we could see whether even the zero-order terms in these equations are correct, and whether the magnitude of the correction is well approximated.

4. Results and Discussion: Spectral Modeling

Following up from the analysis in the previous section, here we discuss the impact of the different constants obtained from Epimetheus using the potentials 18PoZo and 13DaLo on the spectrum produced by Pandora for ozone 666. In particular, we compare our results with high-quality spectra such as the 2020 release from the High Resolution Transmission molecular spectroscopic database (HITRAN 2020).

HITRAN spectra are available from I. E. Gordon et al. (2022) for ozone 666, 668, 686, 667, and 676. For isotopomers 868 and 888, the comparison spectra are obtained from the S&MPO-2020d database (Y. L. Babikov et al. 2014). Isotopomers 688 and 777 do not have spectra available for comparisons, but have been modeled in Section 4.3.

As a brief rundown on the approximate regions of the modes in the spectrum for the isotopologs of ozone; mode 100 is expected to lie within $1050–1150\,cm^{-1}$, mode 010 within $600–800\,cm^{-1}$, and mode 001 within $950–1100\,cm^{-1}$. This gives an order appearance of first mode 010, then mode 001, and finally mode 100 as the wavenumber increases.

4.1. Ozone 666

Ozone 666 is the main isotopolog and a symmetric variant belonging to the point symmetry group C_{2v}. As such, it exhibits bands of either *A* or *B* type for each fundamental mode. Since it is composed entirely of the ^{16}O isotope, spin effects will appear. This means only levels of certain parity will be populated, as explained in J. Flaud & R. Bacis (1998).

Figure 2 compares the spectra produced for the 13DaLo and 18PoZo PES with the HITRAN 2020 data by J.-M. Flaud et al. (1990, 2003), I. E. Gordon et al. (2022), G. Wagner et al.

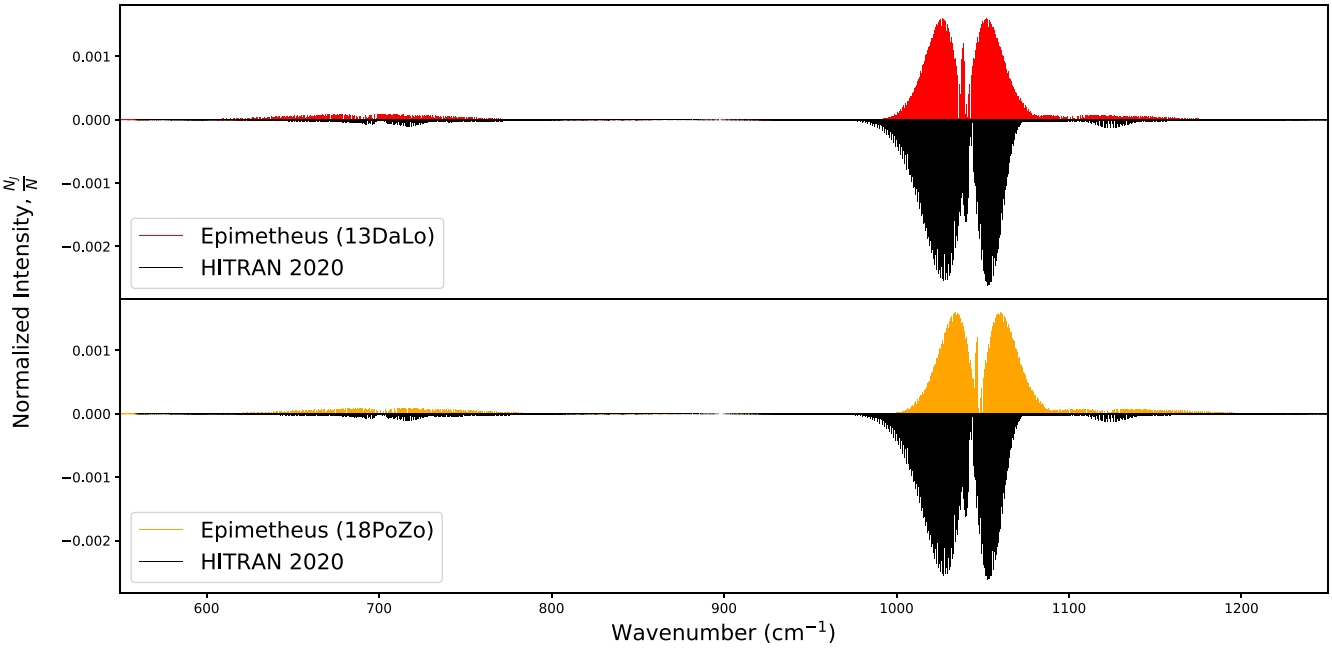

Figure 2. A comparison of the spectra obtained from both potentials from R. Dawes et al. (2013) and O. L. Polyansky et al. (2018) for $^{16}O_3$ using Epimetheus.

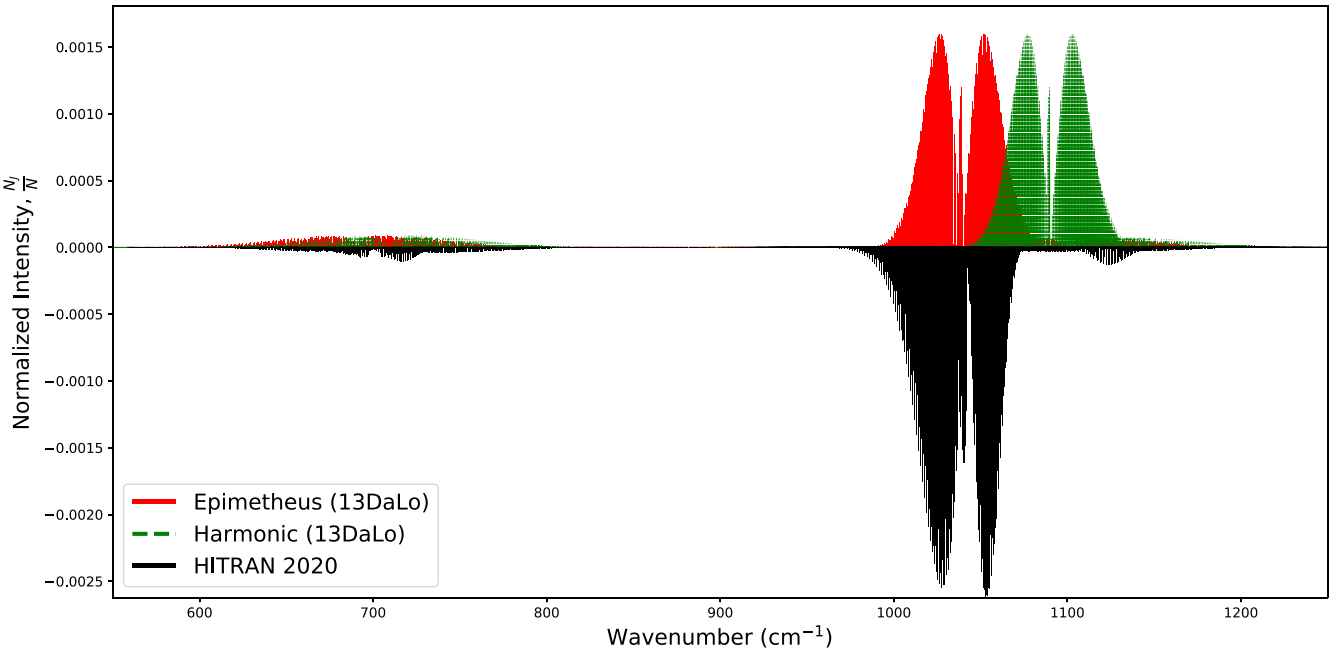

Figure 3. A comparison of the ozone 666 ($^{16}O_3$) spectrum from Epimetheus (13DaLo potential) in green. Data from the HITRAN 2020 release are in black and inverted for comparisons with our results. We have also included a harmonic spectrum also derived from the 13DaLo potential.

(2002), and V. Tyuterev et al. (2021). For this figure (and for all the following figures) HITRAN data are represented as inverted black spectra. The spectrum for 13DaLo reproduces the HITRAN spectrum for the asymmetric stretch mode (001, ν_3) better than the 18PoZo PES, mainly due to a slight band origin shift (of approximately 5 cm^{-1}) for the latter. The bending mode (010, ν_2) is better represented by 18PoZo, whereas neither models the symmetric stretching mode (100, ν_1) accurately. Our spread of the transitions across the spectrum appears to be of similar range to that of HITRAN. Overall, both potentials offer a spectrum which qualitatively reproduces the main features of the HITRAN spectrum.

Owing to a better quantitative match between HITRAN and the spectrum obtained with the 13DaLo PES, particularly for the key mode 001 of the ozone spectrum, we will mainly consider this PES for the remaining figures. It is worth noting that the discrepancy seen for the 18PoZo PES is likely caused by our approximate treatment of anharmonicity rather than the quality of the 18PoZo PES itself, which is not questioned.

In Figure 3, we show that the harmonic approach generates a spectrum that is substantially displaced compared to Epimetheus' anharmonic approach, to the point that modes 100 and 001 in the harmonic approach could easily be confused. For simplicity, we only use for the comparison here the

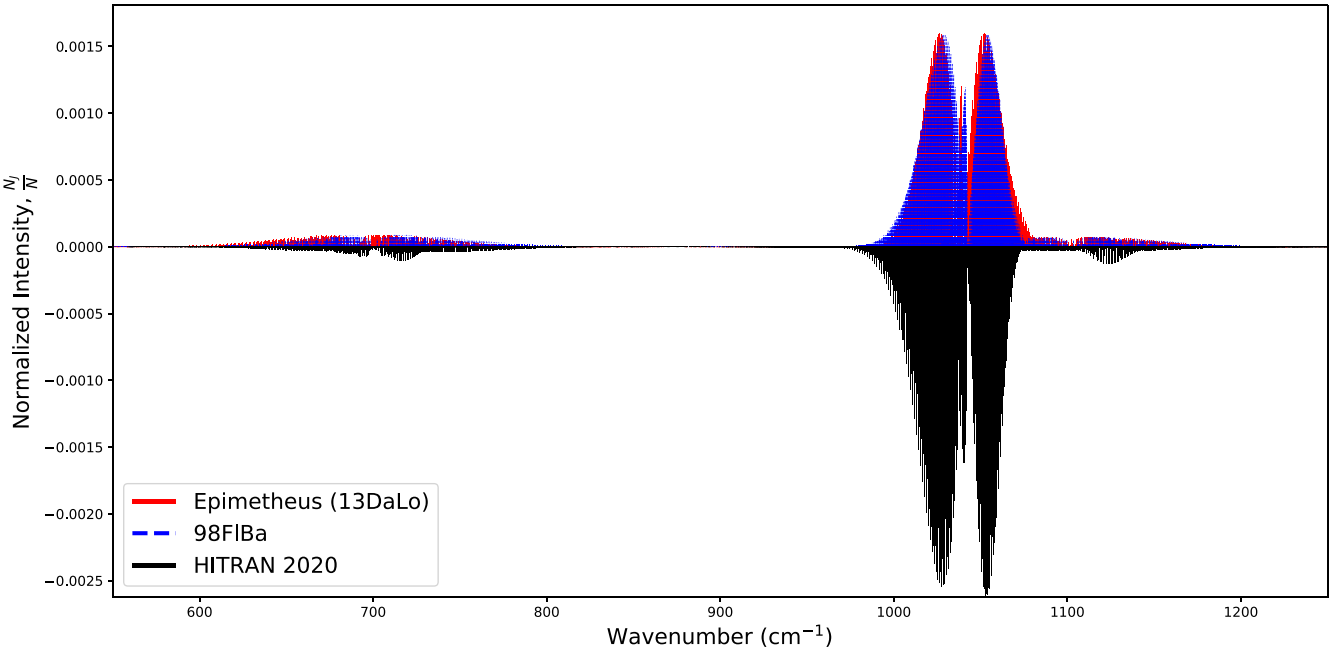

Figure 4. A comparison of the ozone 666 ($^{16}O_3$) spectrum from Epimetheus (13DaLo potential) in red. Data from the HITRAN 2020 release are in black and inverted for comparisons with our results. We have also included a theoretical best result from Epimetheus using literature constants from J. Flaud & R. Bacis (1998) for additional comparisons in blue.

spectrum obtained with the 13DaLo PES. We also note that the harmonic lines for mode 100 are mostly swamped by the 001 mode, presumably due to the large anharmonic correction missing from the harmonic frequency for mode 001. We can see for the bending mode (010) that both methods (TOSH or harmonic) provide similar results, with the Epimetheus method overcorrecting the band origin and the harmonic method naturally underestimating the band origin.

Since the Pandora approach does not account for all rovibrational effects, we test the accuracy of the TOSH (Epimetheus) spectrum by overlaying it with a Pandora spectra that uses the literature constants instead. Indeed, this test uses the same rovibrational simulation approach (Pandora) but highlights the effect caused by small changes of spectroscopic constants on the resulting spectrum. This is shown in Figure 4, where we used constants from J. Flaud & R. Bacis (1998), indicated by the abbreviation 98FlBa. We can see from the figure that the Epimetheus spectrum using both potentials approximates the hypothetical best results of 98FlBa well, however the 13DaLo has a higher fidelity to the asymmetric mode (001). To see the individual spectra for 18PoZo and 13DaLo, please see Figures 12 and 11, respectively. The only major variations occur in the overall breadth of the *R* branch for mode 001 (we can see the red of 13DaLo on both sides of 98FlBa) and the band origin of the bending mode. The increased width of this branch is most likely due to overestimation of the rotational constants, which leads to a wider spread of transitions when used within the branch equation (Equation (20)).

Based on the results shown in Figure 4 and in depth in Figure 5, Pandora can well replicate the HITRAN spectra. Some shortcomings occur, however, especially with mode 100. The shape of this band is not replicated well, and instead of having a single peak our method produces a typical bimodal band. Another difference appears with the bending band, which appears on the HITRAN spectrum to have more of a hybrid band structure (hybrid bands are discussed in more depth later in our results). Our spectral model in this case is limited to a single *B* vibrational band typing for the bending mode.

Regarding the overall relative intensities of the bands, we see that our ratio differs slightly from that of HITRAN, most noticeably the 001 band not having as much weighting. This is something that is not calculated within our code, and relies on the reported literature values for the intensity ratios. In this instance, we have directly taken the ratio of 0.039 (ν_1) : 0.047 (ν_2) : 1 (ν_3) from S. Ivanov & V. Y. Panchenko (1994), which came with no errors. Although intensities are a crucial part of spectra, they are not the focus of this study, hence why we have taken reported relative values for the modes. Through using a normalized intensity, these ratios have proven sufficient in providing us with relative intensities that approximate HITRAN spectra.

4.2. Other Isotopic Variants

We now investigate each of our remaining selected isotopomers by comparing the spectra Pandora is able to produce (using the spectroscopic constants derived by Epimetheus using the 13DaLo potential) and the best experimental data available. The isotopomer spectra have been grouped together into Figures 6 and 7, and each subplot is labeled to indicate which isotopomer it relates to.

Ozone 668 is an asymmetric variant of ozone and therefore belongs to the C_s symmetry group. J. Flaud & R. Bacis (1998) suggested that, for the asymmetric variants, all the vibration-rotation bands are hybrid bands which exhibit both *A*- and *B*-type components. In Pandora, we only model a single band for each mode and use instead the theory for the symmetric variants. We assume that the symmetric component is the dominant contribution to the hybrid bands, which seems justified in practice (Figure 6).

The spectrum for this isotopolog is compared to 668 HITRAN 2020 data by I. E. Gordon et al. (2022), J.-M. Flaud et al. (1990), and A. Barbe et al. (2018), and is shown in Figure 6(A). We see that our spectral modeling reproduces modes 010 (around

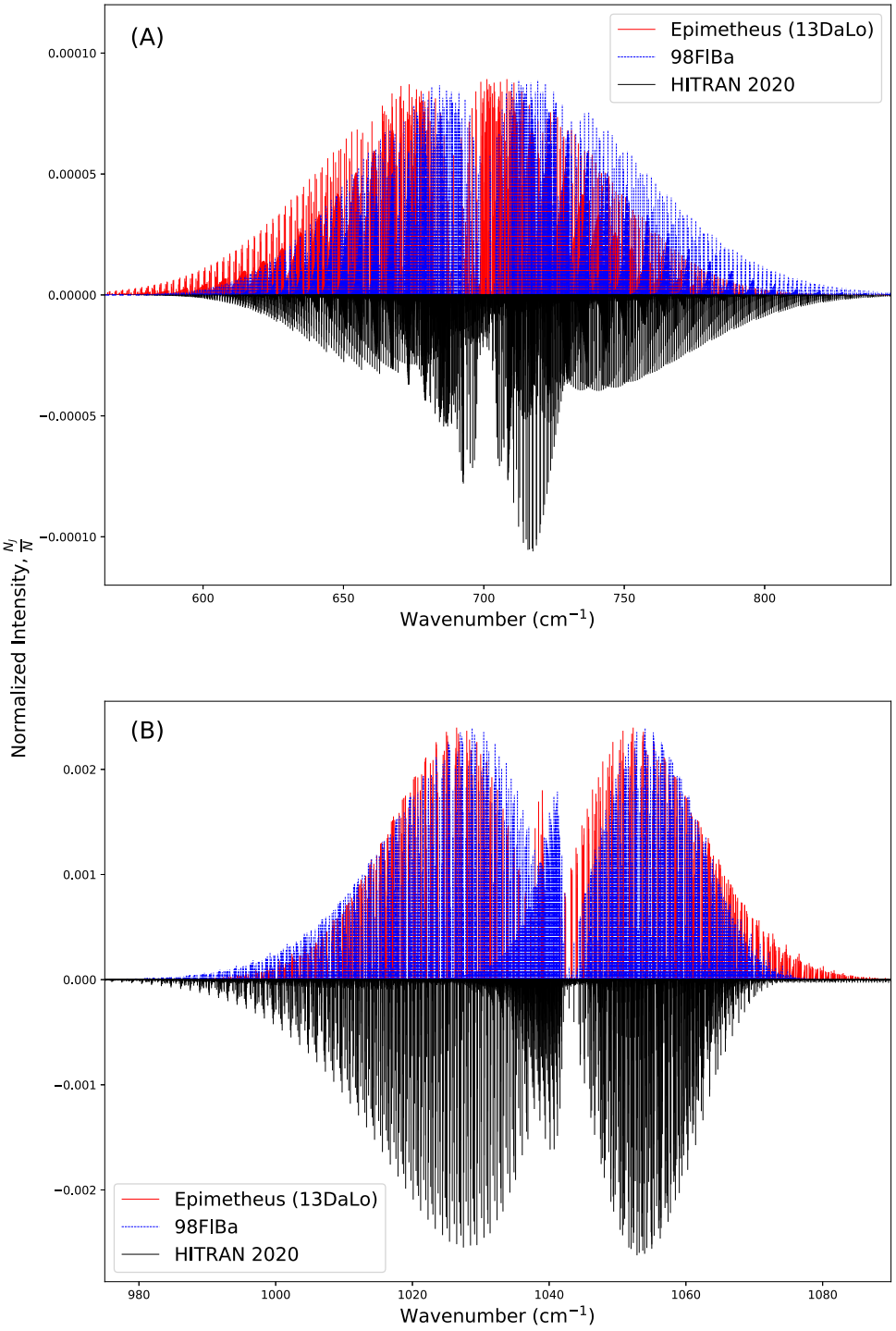

Figure 5. Comparison spectra for the modes of ozone 666 ($^{16}O_3$). Epimetheus (13DaLo potential) is given in red. Data from the HITRAN 2020 release are in black and inverted for comparisons with our results. We have also included a theoretical best result from Epimetheus using literature constants from J. Flaud & R. Bacis (1998) for additional comparisons in blue. (A) shows the spectrum for mode 010, whereas (B) shows the spectrum for mode 001. Mode 100 has been omitted due to its lack of prominence in the spectra.

700 cm^{-1}) and 001 (around 1000–1050 cm^{-1}) quite well; conversely, mode 100 is not as well reproduced.

Our spectral model does not show the same characteristic *PQR* branch as the HITRAN 2020 spectrum, specifically in replicating the small *Q* branch. This is presumably due to the omission of an additional *A* vibrational band, since we only model the *B* type for ν_1. From a qualitative viewpoint, the 100 mode for the Epimetheus *P* branch is mostly swamped by the *R* branch for the 001 mode, something which does not occur for the HITRAN spectrum. This is due to the displacement in our band origin for Epimetheus from the observed frequency. In this particular scenario this is simply a minor issue, as the 100 mode contributes few substantial features to the spectrum.

Moving onto the next ozone isotopolog, 686, we know it is another symmetric ozone variant belonging to the symmetry group C_{2v}. Since this molecule is composed exclusively of ^{16}O and ^{18}O isotopes, spin effects will occur in the spectrum. As was the case for ozone 666, this means only levels of certain

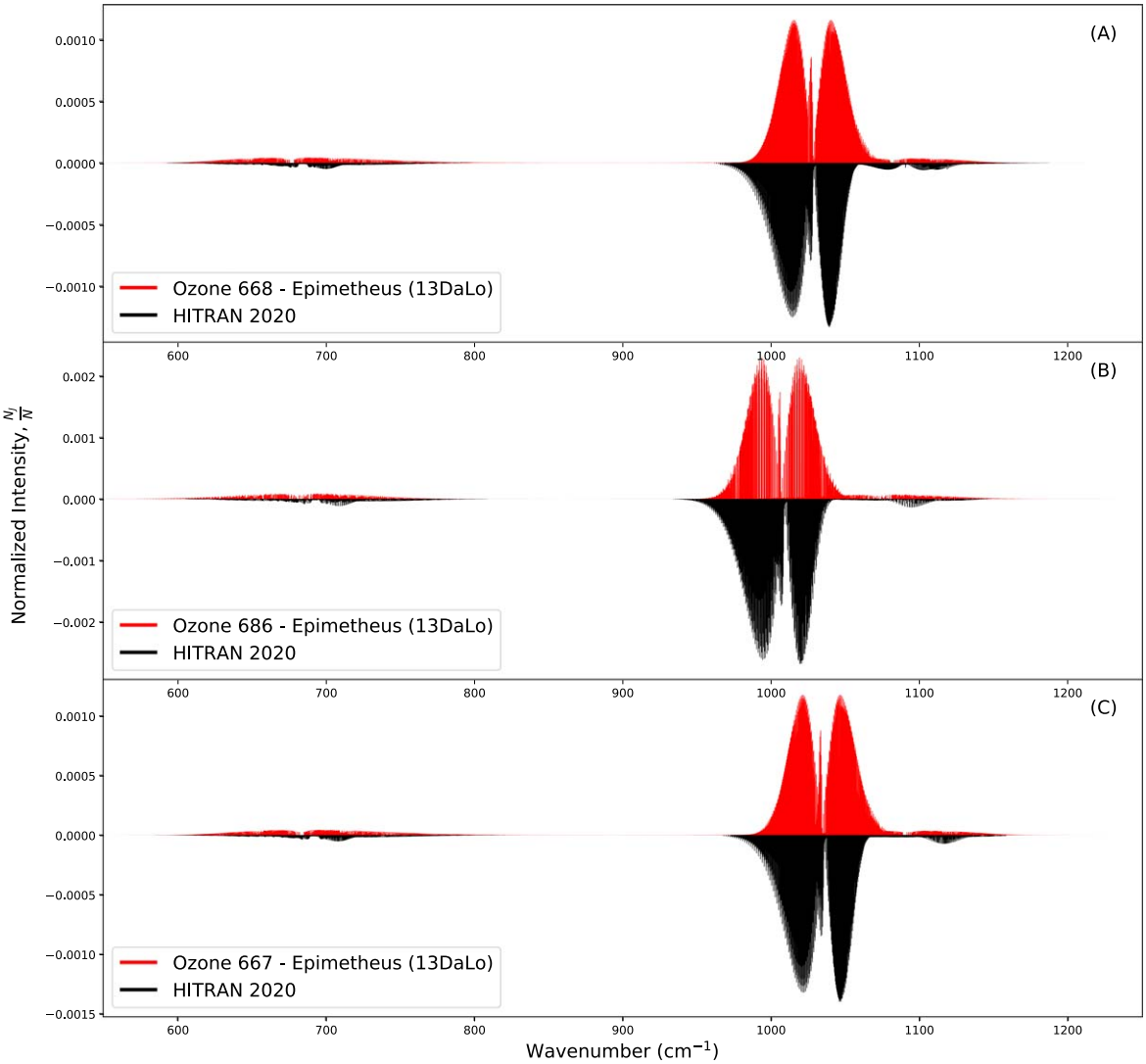

Figure 6. All Epimetheus spectra presented in this graph use the constants derived from the R. Dawes et al. (2013) potential. All graphs compare the Epimetheus spectrum against the data from the HITRAN 2020 release (I. E. Gordon et al. 2022). (A) The graph for ozone 668 ($^{16}O^{16}O^{18}O$). (B) The graph for ozone 686 ($^{16}O^{18}O^{16}O$). (C) The graph for ozone 667 ($^{16}O^{16}O^{17}O$).

parity will be populated. The spectrum for this isotopolog is compared to 686 HITRAN 2020 data from J.-M. Flaud et al. (1990, 2003) and I. E. Gordon et al. (2022), and is shown in Figure 6(B).

The relative ratio of intensities between Epimetheus and HITRAN have a mixed accuracy for 686. The most apparent inaccuracy is for the 001 mode, where the maximum intensity for 686 is approximately half of that of HITRAN. On the other hand, the intensities of the bending mode 010 are well reproduced. While the rotational progression for mode 100 is very weak in our model, the overall shape of modes 010 and 001 agrees with the HITRAN spectrum, with it even displaying some of the same discontinuities that presumably arise from the spin effects.

The next isotopolog discussed is 667, which is an asymmetric variant of ozone and therefore belongs to the C_s symmetry group. The spectrum for this isotopolog is compared to 667 HITRAN 2020 data (C. P. Rinsland et al. 1991; J.-M. Flaud et al. 2003; I. E. Gordon et al. 2022), and is shown in Figure 6(C). Usually, the presence of the ^{17}O isotope leads to a relaxation in population rules (something which has an important effect on the modeling and is discussed further for the 676 isotopomer), but this has no impact as 667 is an asymmetric species. This is because all the sublevels are already populated with the same nuclear spin statistical weight, as detailed in J. Flaud & R. Bacis (1998).

Our ozone 667 spectrum shows a good approximation of the HITRAN spectrum. Some issues with the branch widths are visible, in particular for mode 001, which lies between approximately 1000–1090 cm^{-1}, with a wider the *R* branch. This is due to a slight overestimation of the rotational constants, which prevents the expected rotational branch fold-back. As expected, the 100 mode shape is not reproduced well, but the spread of transitions measure up with relative accuracy.

The first isotopolog shown in Figure 7 is ozone 676 (panel (A)). This isotopolog is compared to 676 HITRAN 2020 data (R. Gamache 1985; L. Rothman et al. 1987; J.-M. Flaud et al. 1990; C. P. Rinsland et al. 1991; G. Wagner et al. 2002; I. E. Gordon et al. 2022) and is another symmetric ozone variant (symmetry group C_{2v}). Since this isotopolog contains the ^{17}O isotope, spin effects are different than if the composition was purely the ^{16}O and/or ^{18}O isotopes. As we

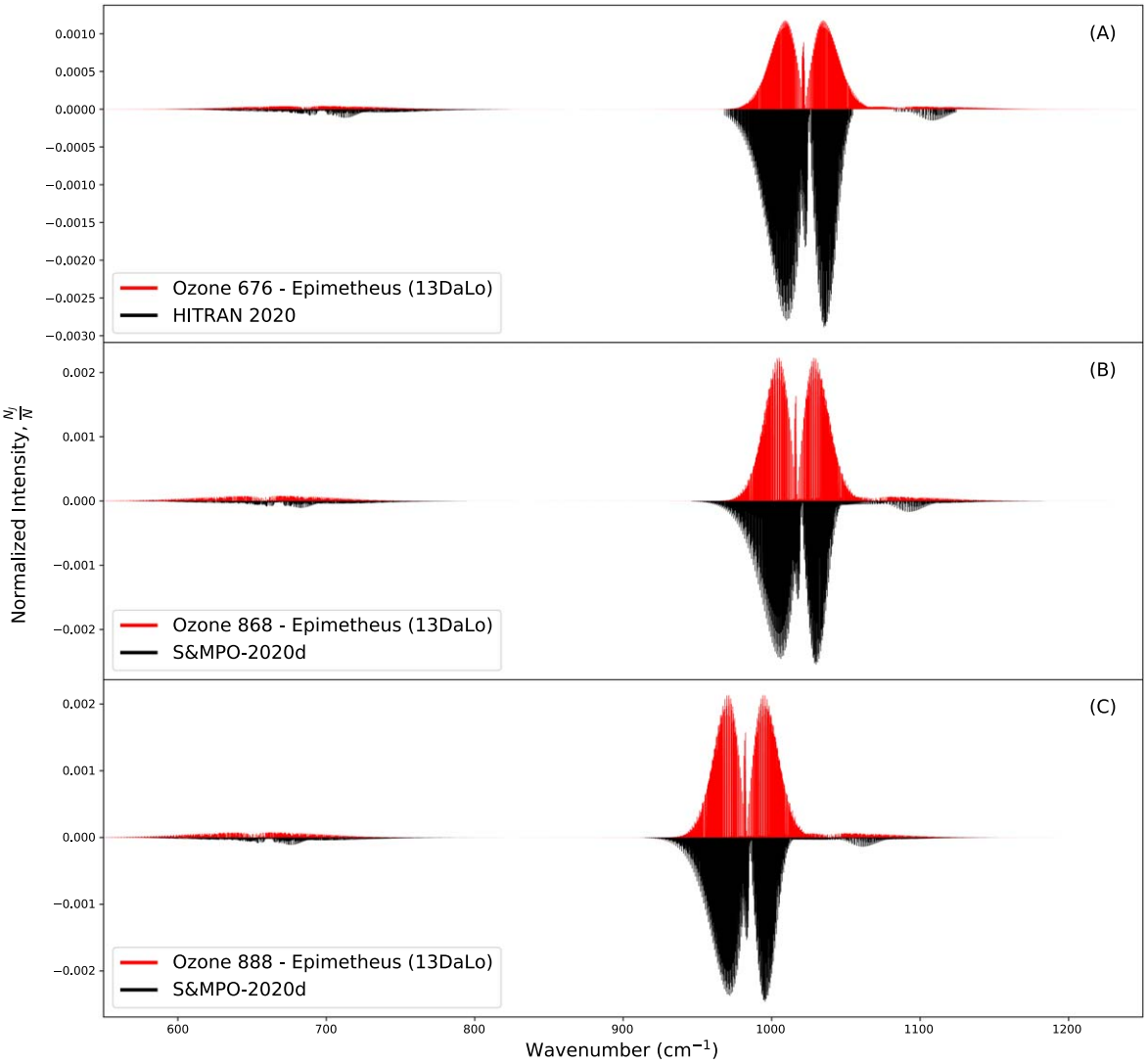

Figure 7. All Epimetheus spectra presented in this graph use the constants derived from the R. Dawes et al. (2013) potential. Graph (A) compares the Epimetheus spectrum against the data from the HITRAN 2020 release (I. E. Gordon et al. 2022), whereas graphs (B) and (C) use the data from the S&MPO-2020d catalog for comparison Y. L. Babikov et al. (2014). (A) The graph for ozone 676 (^{16}O^{17}O^{16}O). (B) The graph for ozone 868 (^{18}O^{16}O^{18}O). (C) The graph for ozone 888 (^{18}O^{18}O^{18}O).

can see in Table 1, the spin for the ^{17}O isotope is nonzero, unlike ^{16}O and ^{18}O. For our approximate method, we have used the assumption that all sublevels of any parity can be populated. However, depending on the parity (odd or even) of the asymmetric mode 001, different types of sublevels gain a different nuclear spin degeneracy (see, e.g., J. Flaud & R. Bacis 1998 for details).

Despite this, for 676 the 001 mode is reproduced quite well in the spectrum shown in the figure. The most notable difference would be the width of the *P* branch, due to the rotational constants not quite matching the target values. As expected from the results of the constants calculated in the previous section, using the 13DaLo potential the origin of the 010 visibly appears to be shifted compared to the HITRAN reference spectrum.

On the other hand, since we have assumed any sublevel can be occupied in 676, we observe an issue with the intensity ratios. This is most noticeable for mode 100, where the general shape of the branches is effectively flattened due to their low ratio value. We can also see that mode 010 is only just visible for the characteristic branch shapes and that mode 001 has a maximum intensity of roughly 0.0010, about 3 times lower than the reference HITRAN data. This is an issue as our spectra would be less prominent than expected for ozone, although still viable, and is presumably a result of our assumptions regarding the sublevels.

As the remaining isotopologs (868 and 888) are similar in composition and symmetry, we will discuss both together in this next section. The species 868 and 888 are shown in panels (B) and (C) of Figure 7, respectively. Due to their compositions only specific sublevels are populated. We see that both simulated spectra provide a good approximation to the reference data. Some discrepancies arise for the 100 mode and there is a slight displacement, roughly 10 cm^{-1}, in band origins for 010. But overall Epimetheus and Pandora combined create spectra of very good likeness to their respective reference data.

4.3. New Ozone Isotopomers

A thorough search of the relevant databases (HITRAN, ExoMol, and JPL) showed no spectra exist for the isotopologs ozone 688 and ozone 777. Additionally, it is worth noting that

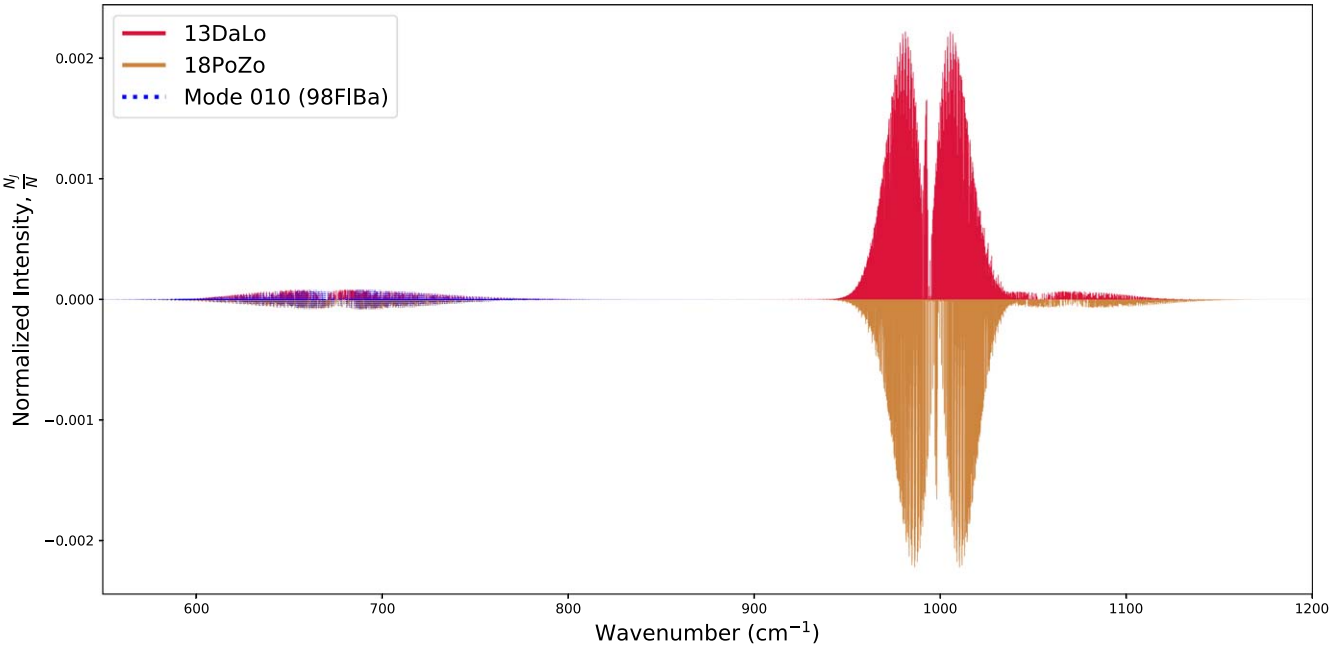

Figure 8. Comparing the spectra for ozone 688 ($^{16}O^{18}O^{18}O$) between the two potentials by R. Dawes et al. (2013, labeled here as 13DaLo) and O. L. Polyansky et al. (2018, labeled here as 18PoZo). The blue spectra have been created in Pandora using constants from J. Flaud & R. Bacis (1998).

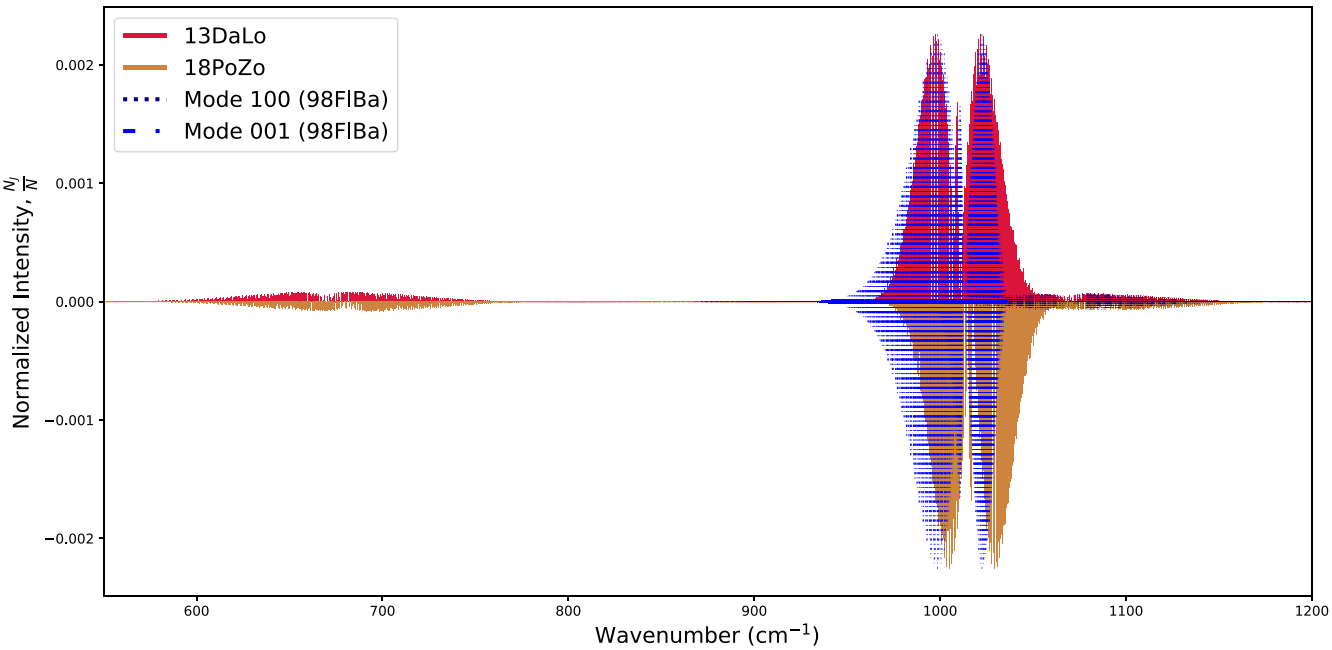

Figure 9. Comparing the spectra for ozone 777 ($^{17}O^{17}O^{17}O$) between the two potentials by R. Dawes et al. (2013, labeled here as 13DaLo) and O. L. Polyansky et al. (2018, labeled here as 18PoZo). The blue and navy spectra have been created in Pandora using constants from J. Flaud & R. Bacis (1998).

it is difficult to create literature-based spectra in Pandora as the data are limited, however where available the literature data have been plotted so some comparisons can be made.

Beginning with 688, Table 4 shows that for 688 only the ground-state rotational constants, the fundamental-mode frequencies, and rotational constants for the 010 mode are available. Only mode 010 of the spectrum can be modeled in Pandora. Figure 8 shows the Epimetheus spectra using the 13DaLo and the 18PoZo potentials for the fundamental modes of ozone 688. The spectrum shows that for the bending mode (010) 13DaLo underestimates the band origin by $\sim$9 cm^{-1} compared to J. Flaud & R. Bacis (1998), whereas 18PoZo has a difference of only $\sim$1 cm^{-1}. Due to the low intensities of this mode, however, this does not appear to make much difference to its qualitative appearance.

For ozone 777 (Table 6), there are now two modes (100 and 001) that can be modeled within Pandora using literature data. Unfortunately, for the bending mode, the band origin and the rotational constants are nonexistent, so it cannot be modeled in Pandora. Figure 9 shows the spectra for 777 using the 13DaLo and the 18PoZo potentials as well as the available literature spectra. The 18PoZo potential spectra reproduce the asymmetric stretch (mode 001) spectra from J. Flaud & R. Bacis (1998) well. The 13DaLo potential only slightly underestimates

the band origin, by $\sim$3 cm^{-1}, whereas 18PoZo overestimates it by $\sim$5 cm^{-1}.

Neither appear to have estimated the upper-mode 001 rotational constants well when compared to the literature. This is shown not only by the 98FlBa *P* branch extending far further into lower wavenumbers but also the weaknesses in reproducing the fold-back characteristic of the 98FlBa *R* branch. Due to the low intensities and its complex appearance, it is difficult to comment on the symmetric stretch (100) mode spectra. Using Table 6, we know that 13DaLo the reproduces the band origin better than 18PoZo, with differences from the literature of 1.6 cm^{-1} and 17.6 cm^{-1}, respectively.

5. Conclusions

Based on our previous work on diatomics (T. M. Cross et al. 2022), we present here the results of a new low-cost computational framework to determine the rotational constants of polyatomic molecules in their vibrational excited states. Our approach leverages and extends the existing TOSH theory from C. Y. Lin et al. (2008) for anharmonic vibrational corrections so it can provide useful geometric corrections. Originally, it was not presumed that this correction would be able to effectively translate from a diatomic theory to polyatomic, but generally we have seen from the data that we can approximate literature constants well.

Overall, we show that the results from our new code Epimetheus approximate the spectroscopic constants for ozone well. It was found that the potential used has a notable impact on the rotational constants calculated by Epimetheus. We have used two different potentials in our analysis, from O. L. Polyansky et al. (2018) and R. Dawes et al. (2013). We find that both potentials provide similar results if the species of ozone is symmetric; however, once asymmetry arises, R. Dawes et al. (2013) struggles to match the accuracy of O. L. Polyansky et al. (2018), by sometimes up to an order of magnitude. Our recommendation therefore would be to use the O. L. Polyansky et al. (2018) potential if the aim is to model all isotopologs with less concern on the accuracy for the asymmetric mode. However, if the 001 mode is of particular concern when modeling, the R. Dawes et al. (2013) potential should be used, much like we have throughout this work.

We have also shown that the band origins, in particular for the symmetric modes, have discrepancies in value from the target literature. The main cause of this issue is the known limitations of the TOSH method. This is due to the fact that the TOSH correction (in particular the σ parameter), as described by C. Y. Lin et al. (2008), comes from the truncated equations of the typical VPT2 theory, and some of the constants, such as η_{iii}, become negligible due to the frameworks of their derivations. However, the strong trends within the anharmonically corrected band origin, discussed in our work, confirms the robustness of our code.

After having validated the results from Epimetheus on the spectroscopic constants of ozone, in forthcoming papers we will provide an extensive library of spectroscopic constants for a comprehensive list of polyatomic molecules. From this study, we primarily supply the spectroscopic constants for the various ozone isotopologs.

Additionally, for this study we have used our new code Pandora to generate molecular spectra, although any software could have been used for the spectral modeling. We show that, in general, our new spectroscopic constants are capable of producing good approximations of the desired spectra for the various isotopologs. In particular, our results produce better approximated spectra than that of the harmonic method, which is often quite inaccurate with respect to band origins and ultimately leads to incorrect branch shapes. This is expected, since its predicted rotational constants remain unchanged upon vibrational excitation.

We have compared our spectral modeling results with the data from HITRAN 2020 and S&MPO-2020d. The main deviations arising due to our method are the following: (i) band origins sometimes have a noticeable displacement from the target spectra, and (ii) some of the details of the spectral features are not correctly predicted. Point (i) naturally arises from the band origin data from the TOSH framework and is not something we control. For point (ii), we have used a simple approximate spectral modeling method that utilizes assumptions to enable low temporal and computational cost. Rather, full complex simulations which use high-resolution methodologies are required to obtain the detailed features of the molecular spectra.

In a forthcoming study, we will discuss Pandora's abilities by assessing its performance with different polyatomic molecules. As the spectra output is useful for the astronomical community, the spectra using Pandora are included within the codes for this paper. Among other upgrades, we will provide the capability to infer the vibrational band types using automation in the code rather than through manual selection, as we did for the current work.

Acknowledgments

We acknowledge the support of JINA-CEE (NSF grant PHY-1430152) and STFC (through the University of Hull's Consolidated grant ST/R000840/1), and ongoing access to `viper`, the University of Hull High Performance Computing Facility. M. P. acknowledges support from the Lendület Program LP2023-10 of the Hungarian Academy of Sciences (Hungary), the ERC Consolidator grant (Hungary) program (RADIOSTAR, grant No. 724560), and the NKFI via K-project 138031 (Hungary). This work was supported by the European Union's Horizon 2020 research and innovation program (ChETEC-INFRA, Project no. 101008324), and the IReNA network supported by US NSF AccelNet. We thank Brad Gibson for proofreading and providing feedback on this manuscript. Additionally, we thank the reviewers for their constructive comments and feedback, which have allowed us to improve this paper.

Code Availability

The Epimetheus code (specifically for ozone) can found on GitHub: https://github.com/CrossTM/Epimetheus_O3. Included with this directory is the Pandora code, which provides the previously detailed spectroscopic modeling. An individual Pandora directory can be found online: https://github.com/CrossTM/PANDORA-TEST. The output files for the data in the Epimetheus code directory are twofold: one is a .csv file, which details all the spectroscopic constants we calculate, while the other is a .txt file, which details the wavelength of a transition and its intensity. We will now briefly outline these files. For example, the file "O3_666_13DaLo_specconst_data.csv" for each mode of ozone 666 details all the harmonic/anharmonic frequencies and ground/upper rotational constants calculated in Epimetheus using the 13DaLo potential. Meanwhile, the file "O3_666_13DaLo_output-data_WN_and_INT.txt" details the wavelength of each transition

for ozone 666 (using 13DaLo) in the first column and the intensity of this transition in the second column.

Appendix A
RCOM Workout

For this entire workout we use a hypothetical molecule $\alpha\beta\gamma$ as the example. This has been done for ease of understanding. First we begin with the COM equation, focusing on the x-coordinate:

$$\boldsymbol{R}_{\mathrm{COM},x} = \frac{(m_\alpha \alpha_x + m_\beta \beta_x + m_\gamma \gamma_x)}{m_\alpha + m_\beta + m_\gamma}, \tag{A1}$$

where α_x, β_x, and C_x represent the x-coordinates of the α, β, and γ atom, respectively (see also Figure 10). We then continue this for the y- and z-coordinates:

$$\boldsymbol{R}_{\mathrm{COM},y} = \frac{(m_\alpha \alpha_y + m_\beta \beta_y + m_\gamma \gamma_y)}{m_\alpha + m_\beta + m_\gamma}, \tag{A2}$$

$$\boldsymbol{R}_{\mathrm{COM},z} = \frac{(m_\alpha \alpha_z + m_\beta \beta_z + m_\gamma \gamma_z)}{m_\alpha + m_\beta + m_\gamma}. \tag{A3}$$

We now compile the various $\boldsymbol{R}_{\mathrm{COM},n}$ elements into an array:

$$\boldsymbol{R}_{\mathrm{COM}} = \begin{bmatrix} R_{\mathrm{COM},x} \\ R_{\mathrm{COM},y} \\ R_{\mathrm{COM},z} \end{bmatrix}. \tag{A4}$$

To then calculate the position of an atom in the molecule (in this example we take the α atom), we take away the $\boldsymbol{R}_{\mathrm{COM}}$ positions from the origin positions:

$$\boldsymbol{r}_{\mathrm{COM},\alpha} = \begin{bmatrix} \alpha_x \\ \alpha_y \\ \alpha_z \end{bmatrix} - \begin{bmatrix} R_{\mathrm{COM},x} \\ R_{\mathrm{COM},y} \\ R_{\mathrm{COM},z} \end{bmatrix}. \tag{A5}$$

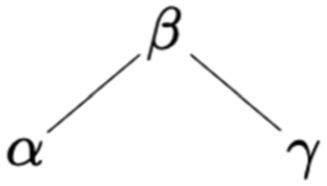

Figure 10. Depiction of the 2D chemical structure of an imaginary molecule $\alpha\beta\gamma$.

This ultimately gives us the COM position for the α atom. This process needs to be repeated for β and γ.

Appendix B
Inertia Tensor Components

For completeness, we provide here the formulae employed for the various elements of the inertia tensor detailed in Section 2.3, where m_i represents the mass:

$$I_{xx} = \sum_i m_i (y_i^2 + z_i^2), \tag{B1}$$

$$I_{yy} = \sum_i m_i (x_i^2 + z_i^2), \tag{B2}$$

$$I_{zz} = \sum_i m_i (x_i^2 + y_i^2), \tag{B3}$$

$$I_{xy} = I_{yx} = -\sum_i m_i x_i y_i, \tag{B4}$$

$$I_{xz} = I_{zx} = -\sum_i m_i z_i y_i, \tag{B5}$$

$$I_{yz} = I_{zy} = -\sum_i m_i y_i z_i. \tag{B6}$$

Appendix C
Additional Spectra

Spectra for ozone 666 ($^{16}O_3$) using 13DaLo (Figure 11) and 18PoZo (Figure 12).

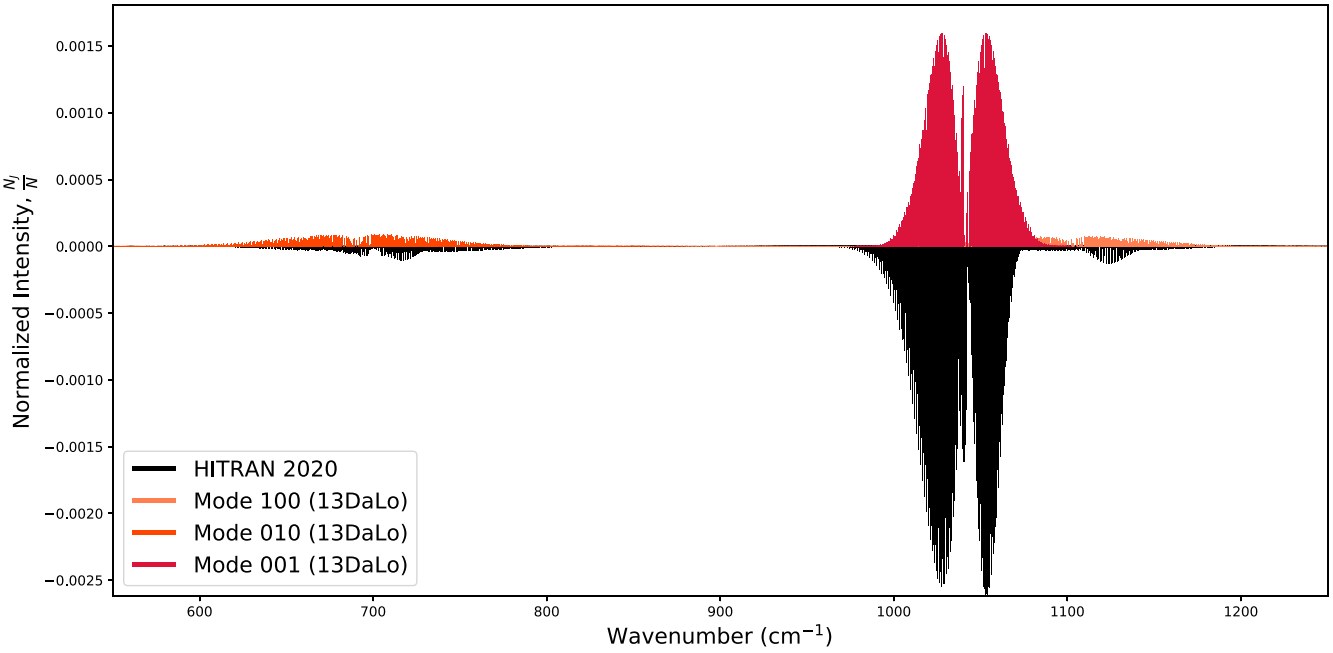

Figure 11. Spectra for the modes of ozone 666 ($^{16}O_3$) using 13DaLo, given in red. Data from the HITRAN 2020 release are in black and inverted for comparisons with our results.

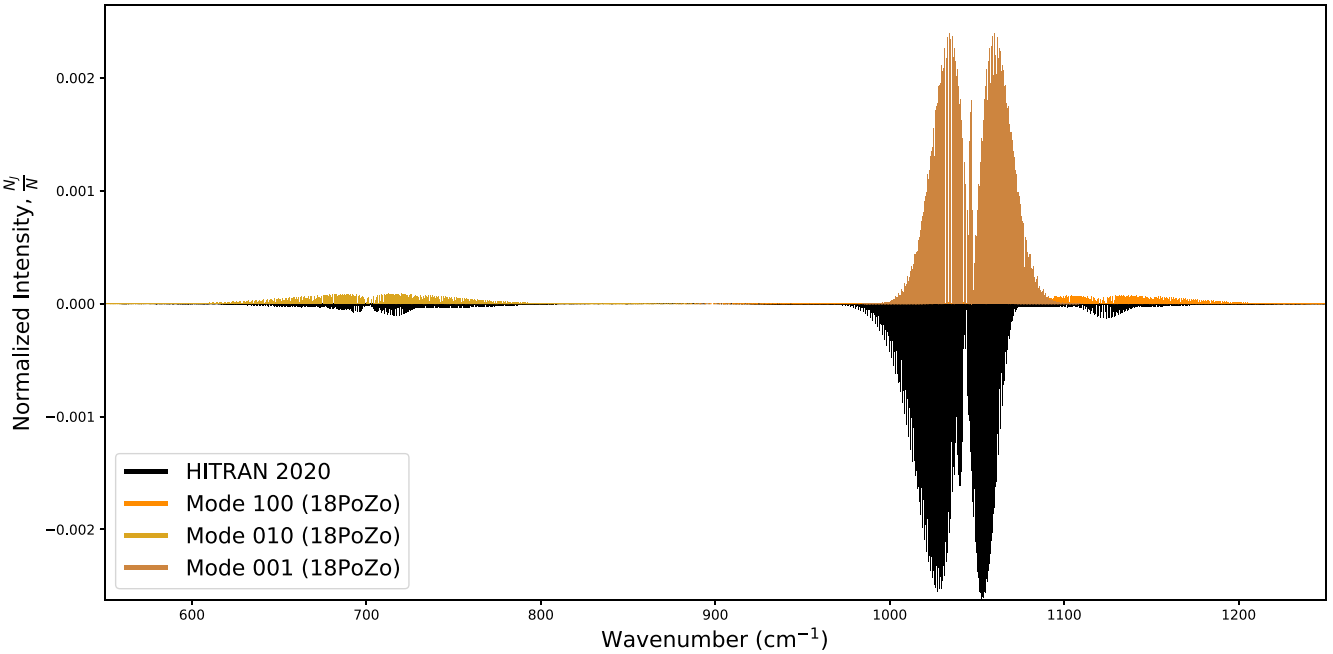

Figure 12. Spectra for the modes of ozone 666 ($^{16}O_3$) using 18PoZo, given in red. Data from the HITRAN 2020 release are in black and inverted for comparisons with our results.

ORCID iDs

Thomas M. Cross https://orcid.org/0000-0001-6621-8182
David M. Benoit https://orcid.org/0000-0002-7773-6863
Marco Pignatari https://orcid.org/0000-0002-9048-6010

References

Allen, H. C., & Cross, P. C. 1963, Molecular Vib-rotors: The Theory and Interpretation of High Resolution Infra-red Spectra (New York: Wiley), 324
Åstrand, P.-O., Ruud, K., & Taylor, P. R. 2000, JChPh, 112, 2655
Babikov, Y. L., Mikhailenko, S. N., Barbe, A., & Tyuterev, V. G. 2014, JQSRT, 145, 169
Banwell, C. N. 1972, Fundamentals of Molecular Spectroscopy (2nd ed.; New York: McGraw-Hill), 348
Barbe, A., Mikhailenko, S., Starikova, E., & Tyuterev, V. 2022, Molecules, 27, 911
Barbe, A., Secroun, C., & Jouve, P. 1974, JMoSp, 49, 171
Barbe, A., Starikova, E., De Backer, M. R., & Tyuterev, V. G. 2018, JQSRT, 218, 231
Battistuzzi, M., Cocola, L., Claudi, R., et al. 2023, FrPS, 14, 1070359
Carney, G. D., Sprandel, L. L., & Kern, C. W. 1978, Variational Approaches to Vibration-rotation Spectroscopy for Polyatomic Molecules, Vol. X (New York: Wiley), 305
Chapman, S. 1930, The London, Edinburgh, and Dublin Philosophical Magazine and Journal of Science, 10, 369
Cooke, S. A., & Ohring, P. 2013, J. Spectrosc., 2013, 1
Cross, T. M., Benoit, D. M., Pignatari, M., & Gibson, B. K. 2022, ApJ, 925, 57
Dawes, R., Lolur, P., Li, A., Jiang, B., & Guo, H. 2013, JChPh, 139, 201103
Domagal-Goldman, S. D., Segura, A., Claire, M. W., Robinson, T. D., & Meadows, V. S. 2014, ApJ, 792, 90
Dundas, K. O. H. M., Beerepoot, M. T. P., Ringholm, M., et al. 2021, JCTC, 17, 3599
Erba, A., Maul, J., Ferrabone, M., et al. 2019, JCTC, 15, 3755
Fast, K. E., Kostiuk, T., Lefèvre, F., et al. 2009, Icar, 203, 20
Field, R. W. 2015, Rotation of Polyatomic Molecules (Cham: Springer), 69
Flaud, J., & Bacis, R. 1998, AcSpA, 54, 3
Flaud, J.-M., Camy-Peyret, C., Rinsland, C. P., Smith, M. A., & Devi, V. M. 1990, Atlas of Ozone Spectral Parameters from Microwave to Medium Infrared (New York: Academic)
Flaud, J.-M., Piccolo, C., Carli, B., et al. 2003, OpAtO, 16, 194
Gamache, R. 1985, JMoSp, 114, 31
Gayday, I., Teplukhin, A., Kendrick, B. K., & Babikov, D. 2020, JChPh, 152, 144104
Golden, S. 1948, JChPh, 16, 78
Gordon, I. E., Rothman, L. S., Hargreaves, R. J., et al. 2022, JQSRT, 277, 107949
Greaves, J. S., Richards, A. M., Bains, W., et al. 2020, NatAs, 5, 655
Grenfell, J., Gebauer, S., Godolt, M., et al. 2013, AsBio, 13, 415
Harman, C. E., & Domagal-Goldman, S. 2018, in Handbook of Exoplanets, ed. H. J. Deeg & J. A. Belmonte (Cham: Springer), 3203
Hathorn, B. C., & Marcus, R. A. 2001, JPCA, 105, 5586
Hennig, P., & Strey, G. 1976, ZNatA, 31, 244
Herzberg, G. 1945, Molecular Spectra and Molecular Structure. Vol. 2: Infrared and Raman Spectra of Polyatomic Molecules (New York: Van Nostrand, Reinhold)
Hino, O., Kinoshita, T., Chan, G. K.-L., & Bartlett, R. J. 2006, JChPh, 124, 114311
Ivanov, S., & Panchenko, V. Y. 1994, Uspekhi Fizicheskih Nauk, 164, 725
Kaltenegger, L. 2011, in Encyclopedia of Astrobiology, ed. M. Gargaud, R. Amils, J. Cernicharo Quintanilla et al. (1st ed.; Berlin: Springer), 122
King, G. W., Hainer, R. M., & Cross, P. C. 1943, JChPh, 11, 27
Lee, T. J., & Scuseria, G. E. 1990, JChPh, 93, 489
Lefèvre, F., Trokhimovskiy, A., Fedorova, A., et al. 2021, JGRE, 126, e06838
Lin, C. Y., Gilbert, A. T. B., & Gill, P. M. W. 2008, Theor. Chem. Acc., 120, 23
Marais, D. J. D., & Walter, M. R. 1999, AnRES, 30, 397
Marcq, E., Baggio, L., Lefèvre, F., et al. 2019, Icar, 319, 491
Mikhailenko, S., Barbe, A., Tyuterev, V., & Chichery, A. 1999, AtOO, 12, 771
Montmessin, F., Bertaux, J.-L., Lefèvre, F., et al. 2011, Icar, 216, 82
Noll, K. S., Johnson, R. E., Lane, A. L., Domingue, D. L., & Weaver, H. A. 1996, Sci, 273, 341
Ochterski, J. W. 1999, White paper: Vibrational Analysis in Gaussian
Olsen, K. S., Lefèvre, F., Montmessin, F., et al. 2020, A&A, 639, A141
Polyansky, O. L., Zobov, N. F., Mizus, I. I., et al. 2018, JQSRT, 210, 127
Prinn, R. G., Alyea, F. N., & Cunnold, D. M. 1978, AREPS, 6, 43
Rinsland, C. P., Smith, M. A., Malathy Devi, V., et al. 1991, JMoSp, 149, 474
Rothman, L., Gamache, R., Goldman, A., et al. 1987, ApOpt, 26, 4058
Schwieterman, E. W., Kiang, N. Y., Parenteau, M. N., et al. 2018, AsBio, 18, 663
Seager, S., Bains, W., & Petkowski, J. J. 2016, AsBio, 16, 465
Segura, A., Meadows, V. S., Kasting, J. F., Crisp, D., & Cohen, M. 2007, A&A, 472, 665
Solomon, S. 1999, RvGeo, 37, 275
Spiegel, M., Semidalas, E., Martin, J. M. L., Bentley, M. R., & Stanton, J. F. 2023, MolPh, 122, e2252114
Tennyson, J., Yurchenko, S. N., Al-Refaie, A. F., et al. 2020, JQSRT, 255, 107228
Tyuterev, V., Barbe, A., Mikhailenko, S., Starikova, E., & Babikov, Y. 2021, JQSRT, 272, 107801
Wagner, G., Birk, M., Schreier, F., & Flaud, J. M. 2002, JGRD, 107, 4626
Zapata Trujillo, J. C., Pettyjohn, M. M., & McKemmish, L. K. 2023, MNRAS, 524, 361